Challenge Journal of STRUCTURAL MECHANICS

Vol.9 No.3 (2023)

auxetic building codes compressive strength dynamic analysis earthquake finite element analysis finite element method girder bridge mechanical properties metaheuristic algorithms modal analysis optimization prestresing pushover analysis reinforced concrete seismic design shallow foundations smart concrete steel structures structural dynamics temperature effects thick plate wind

ISSN 2149-8024

TULPAR ACADEMIC PUBLISHING

Challenge Journal of Structural Mechanics

E-mail: *cjsmec@challengejournal.com*

Web page: *cjsmec.challengejournal.com*

TULPAR Academic Publishing
www.tulparpublishing.com

Challenge Journal of Structural Mechanics

CONTENTS

Research Articles

TULPAR ACADEMIC PUBLISHING

Challenge Journal of Structural Mechanics

Research Article

Effect of dosage on the mechanical properties of epscrete

Mehmet Canbaz [a,*], Emir Günaltılı [a], Uğur Albayrak [a]

[a] *Department of Civil Engineering, Eskişehir Osmangazi University, 26480 Eskişehir, Türkiye*

ABSTRACT

Epscrete, which is made by employing aggregate made of expanded polystyrene beads, is often used to make wall panels, block components, and insulating plates. For these products to have greater mechanical qualities, 400, 600, and 800 dose epscrete specimens were made in this research, which also considered the influence of cement quantity. The water-cement ratio was considered to be 0.5. In addition to the reference specimens, the same manufacture was carried out utilizing a 1% plasticizer admixture. Specimens were subjected to unit weight, ultrasonic pulse, water absorption, bending, and comprehension tests 7 and 28 days after production. The effects of the dose and plasticizer rate on the physical and mechanical properties of early and ultimate epscrete specimens were determined according to the unit weight, ultrasonic pulse velocity, water absorption rates, bending and compressive strength values. Increasing the dosage increased the ultrasonic pulse velocity, reduced water absorption by reducing the amount of gap and reduced water absorption, and increased compressive strength by approximately 65 % and bending strength by about 60 %. It has been determined that the mechanical and physical properties of epscrete are affected by dose and mixture ratios. By increasing the dosage, it has been seen that carrier light carrier blocks can be obtained.

ARTICLE INFO

Article history:
Received 15 December 2022
Revised 29 January 2023
Accepted 8 May 2023

Keywords:
Epscrete
Dosage
Physical properties
Mechanical properties
Lightweight block

1. Introduction

Expanded polystyrene (EPS) blocks can be used for thermal insulation and lightening the structure against seismic effects as Rauf et al. (2011), Mohammed and Zain (2016) and Miled et al. (2004) stated in their studies. However, as Uygunoğlu et al. (2015), the flammability of these materials limits their use. According to Li et al. (2018) and Babu et al. (2006), granules forming EPS blocks are polymers with closed cell structure, high air content, hydrophobic structure, and low density. For this reason, EPS granules can be used in the production of lightweight concrete as noted by Tang et al. (2008). Concrete in which EPS beads are used as aggregate is called EPS concrete. As a result of the cement paste covering the EPS granules, the material becomes incombustible. In this state, it can be used in many areas such as thermal insulation material, floating marine structures, geogrid, and road barrier as used by Gyawali (2023). However, the freeze-thaw resistance of EPS concrete is low. For this reason, in order to increase the freeze-thaw resistance, antifreeze and silane bonding agent can be applied to the outside of the EPS concrete, as well as EPS can be modified by wrapping the EPS surface with high performance materials, and polyvinyl alcohol and fiber can be added to the mixture by Yuan et al. (2022). Since EPS-based lightweight concrete panels reduce energy consumption by up to 40%, they can reduce carbon emissions by up to 20% as Meddage et al. (2022) stated in their studies. At the same time, it reduces the use of cement and reduces carbon emissions from cement production. According to Prasittisopin et al. (2022) and Xiang et al. (2022), since EPS particle content increases the porosity, it reduces the strengths by up to 45%, while increasing the dynamic performance and improving the fatigue properties. When the stress-strain curves of EPS concrete obtained under axial compression load are examined, firstly, a linear elongation and small cracks form on the surface, while in the collapsed stage, the increase in stress concentration at the interface of EPS beads and

* *Corresponding author*. Tel.: +90-222-239-3750 ; Fax: +90-222-239-3613 ; E-mail address: mcanbaz@ogu.edu.tr (M. Canbaz)
ISSN: 2149-8024 / DOI: https://doi.org/10.20528/cjsmec.2023.03.001

cement leads to the formation of new cracks due to the low strength of the beads. Feng et al.'s (2022) study revealed that concrete loses its bearing capacity during the stress softening phase. When the drying shrinkage of EPS aggregate concrete is examined by Maghfouri et al. (2022), it was observed that EPS cannot resist shrinkage due to its low rigidity increases drying shrinkage. According to Assaad et al. (2022), If waste EPS insulation materials are used instead of aggregate in the production of lightweight reinforced concrete beams, their shear strength decreased by up to 20%. There are studies prepared by Mahmoud et al. (2023) where EPS bead wastes are used for insulation purposes in the production of geopolymer concrete. It has been determined by Vinod et al. (2022) that EPS beads have higher compressive strength than clay bricks and lower than traditional porous blocks when used in foam concrete block production. If EPS is wrapped in airgel, its compressive strength can increase up to 137% as Jiang et al. (2022) stated in their papers. In studies like Rosca and Serbanoiu (2022), using EPS by volume instead of aggregate, the compressive strength increased as the aggregate particle size decreased, as well as the EPS bead distribution became more uniform. In a study by Sadrmomtazi et al. (2012), in which EPS granules were used as aggregate, the strength increased with the use of silica fume, while the strength decreased with the use of rice husk ash. It has been observed that homogeneity and slenderness are important in studies where fracture is modeled in concretes using CT scanning to obtain the micromorphology of concretes with EPS aggregates. According to Feng et al. (2022), these data provide improvement regarding the design, construction and cure of EPS concrete.

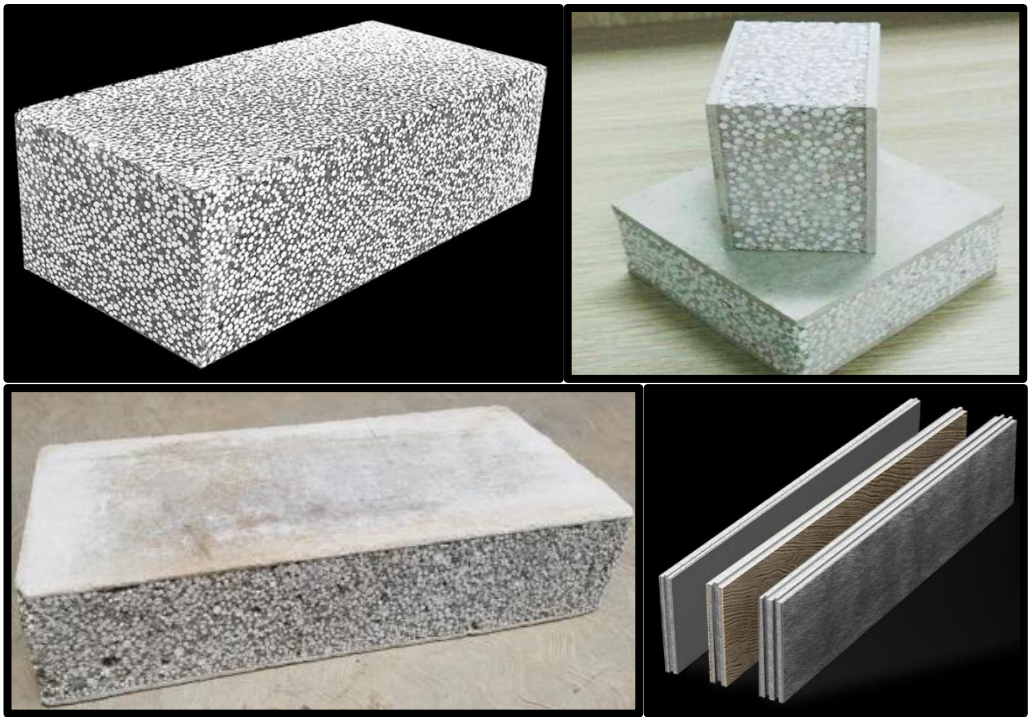

Fig. 1. Epscrete types used in the application (Susilorini et al. 2020; Mishra and Dashore 2020).

As can be seen from Fig. 1, there are a variety of EPS products available, including wall panels, block elements, and insulation plates. There have been previous studies on the strength and durability of epscrete products. In this study, unlike previous studies, a higher amount of cement was added in different proportions and aimed to have higher mechanical properties as well as lighter ones. For this purpose, 400, 600, and 800 dosage epscrete specimens were produced using EPS beads. Here, 400 doses can be used in light concrete applications in general. Therefore, 400 doses were chosen as a reference. If the dosage is increased too much, the upper limit is limited to 800, as there may be too many problems due to the heat of hydration as well as the cost. 600 doses were taken as an intermediate value. Unit weight, ultrasonic pulse, bending, and compressive strength tests were performed on these specimens and their mechanical and physical properties were determined.

2. Experimental study

2.1. Materials

Cement: Type R CEM I 42.5 cement was used in the mixtures. The properties of this cement are given in Table 1.
Aggregate: EPS beads were used as an aggregate in mixtures. The properties of the beads were listed in Table 2.
Water: Municipal water was used in the mixtures. Properties of the mix-water is given in Table 3.
Admixture: The superplasticizer (SP) was mixed as an admixture in a lightweight concrete design. Admixture properties were given in Table 4.

Table 1. Properties of cement.

Chemical content, mg/dm³									
CaO	Al_2O_3	SiO_2	Fe_2O_3	MgO	Cl-	Na_2O	K_2O	LOI	SO_3
62.9	4.56	19.19	3.09	1.88	0.013	0.31	0.63	3.8	3.21
Physical properties									
Specific surface cm²/g		Expansion, mm		Initial setting, min.		Final setting, min.		Density, g/cm³	
3590		1		163		227.5		3.09	

Table 2. Properties of EPS beads.

Diameter range, mm	Unit Weight, kg/m³	Density, kg/m³
1.5-3.0	20	60

Table 3. Properties of water.

Cu	Mn	Al	NH_4	Fe	NO_3	K	Ni	As	Conductivity, µS/cm	pH	Hardness, Fd⁰
0.016	0.015	0.04	0.06	0.007	11.1	6.8	5.07	1.19	628	7.35	30.11

Table 4. Properties of plasticizer.

Content	Structure	Colour	Density	pH	Cl-	Alkali
Modified lignosulfonate	homogeneous, liquid	dark brown	1.135 kg/dm³	8	<0.1%	<7 %

2.2. Method and tests

In lightweight concrete containing EPS beads (epscrete) production, the water-cement ratio was taken into account as 0.5. Specimens were taken from the epscrete mixtures prepared according to the mixing ratios given in Table 5 into prismatic molds with dimensions of 4x4x16 cm. The specimens taken from the mold one day later were kept under standard curing conditions until the day of the experiments. Unit weight, ultrasonic pulse, water absorption, splitting tensile, compression and bending tests were carried out on specimens 7 and 28 days after production are showed in Fig. 2.

Table 5. Mixture ratio, kg/m³.

Cement	Water	EPS beads	Admixture (SP)
400	200	20	0
400	200	20	4
600	300	20	0
600	300	20	6
800	400	20	0
800	400	20	8

3. Discussion

The unit weight changes of the epscrete specimens are given in Fig. 3. According to Fig. 3, the unit weights ranged between 0.6 and 1.4 kg/dm³. A decrease in the dosage from 800 kg to 600 kg reduced the unit weights of the specimens by 24%, while a decrease of 400 kg in the dosage caused the unit weights of the specimens to decrease by 51%. The heaviest component in the epscrete composition is cement. Due to the fact that the other components are quite light compared to cement, the change in the amount of cement caused a significant change in the unit weight of the specimens. Since better placement was achieved by adding a plasticizer to the mixture, an increase in the unit weights of the specimens was observed, reaching 5.7%. It was determined that the unit weights of the specimens were higher due to the low water loss in the early ages, and these values decreased by 8% in 28 days. When the studies of Kuhail (2001), Jayanth and Sowmya (2018) are examined, the unit weights of the epscrete samples using 400 doses of cement are reduced to 0.95 kg/dm³, similar to this study, while the unit weights can reach up to 1.27 kg/dm³ in the case of using 600 doses of cement (Kuhail 2001; Jayanth 2018).

The ultrasonic pulse velocity values of epscrete specimens varies with dosage were shown in Fig. 4. The determination of ultrasonic pulse velocity can provide information about the quality of the concrete by changing the speed as a result of the change in path required for vibration progression depending on the void structure and amount of space in the sample. However, in this study, the presence of EPS beads as well as voids and cement paste in the inner structure was effective in the propagation of the vibration created by the piezoelectric material. Vibration does not propagate in pores, but circulates around it. Hardened cement paste and EPS grains are different types of materials. Cement paste is a ceramic material while EPS is a polymer material. However, since it is an expanded polymer. It contains gaps in

its internal structure and thus can slow down the progression of vibration, therefore, reducing ultrasonic pulse velocity values. In Fig. 4, it was observed that as the dosage increased, the ultrasonic pulse velocity values increased by 78%. Since the admixture provides better placement, it has reduced the voids and increased the ultrasonic pulse velocity values by up to 20%. The increase in solid structures as a result of the continuation of hydration over time caused an increase in ultrasonic pulse velocity values of up to 14%.

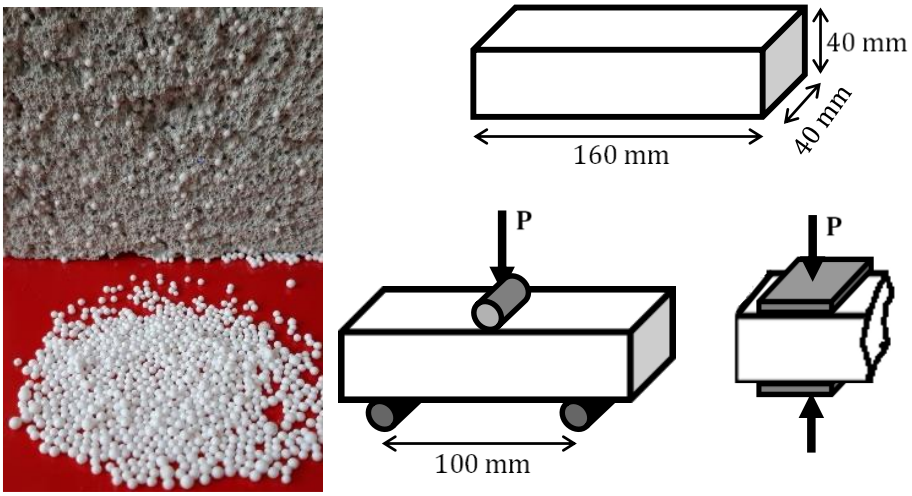

Fig. 2. Mixture, EPS beads, schematic draw of specimens and tests.

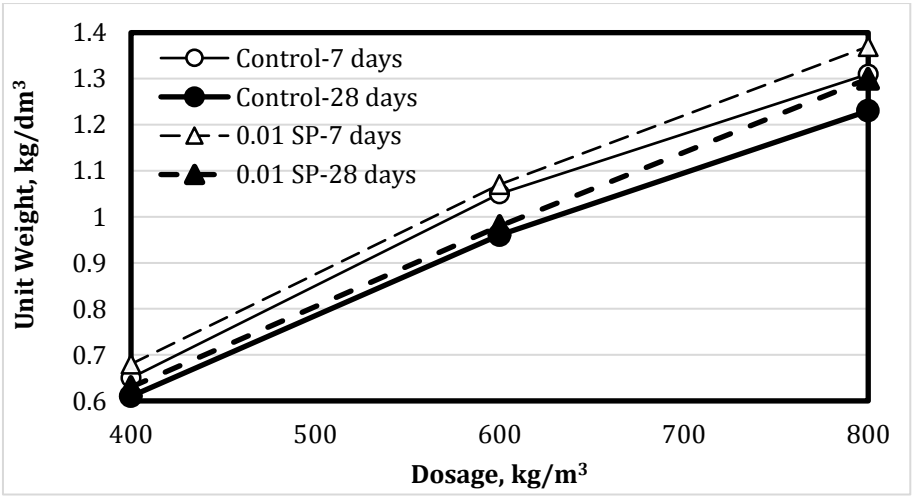

Fig. 3. The effect of dosage on unit weights of epscrete.

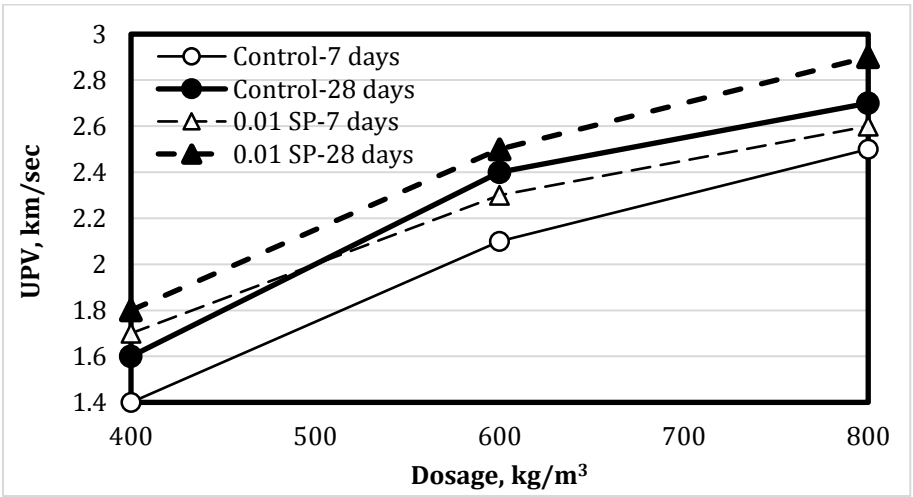

Fig. 4. Ultrasonic pulse velocity change of epscrete with dosage.

The water absorption test results of the produced epscrete specimens 7 and 28 after the production are shown in Fig. 5. It was seen that the water absorption rates by weight ranged between 3 and 14 percent. The capillary voids, micro and macro voids in the cement paste were effective in absorbing water due to the water absorption and impermeability of the EPS grains. Therefore, the water absorption rate of the specimens decreased by 67% as a result of the decrease in voids with the increase in dosage. The increase in machinability with the addition of admixtures caused a decrease in macro voids and thus a decrease in water absorption rates of up to 12%. In addition, the increase in the microstructure of the CSH structures formed as a result of cement hydration over time caused a decrease in water absorption rates of up to 36%. In previous studies as Jayanth and Sowmya (2018), unlike this study, UPV values were found to be higher, such as 2.64 km/sec, since sand was used.

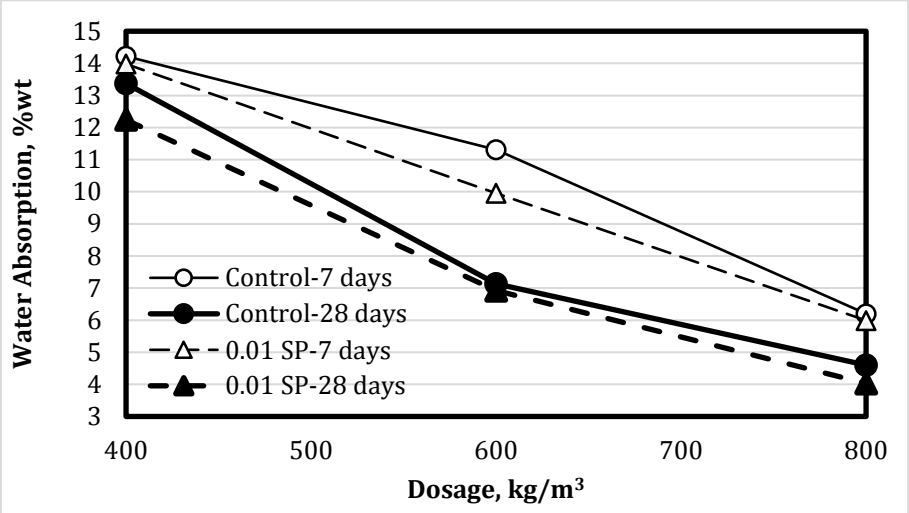

Fig. 5. Water absorption of epscrete.

The bending strength changes determined as a result of the bending test performed on epscrete specimens are shown in Fig. 6. When Fig. 6 was examined, the decrease in dosage in the production of epscrete caused a decrease in the bending strength of the specimens, reaching 40%. The increase in dosage, the better filling of the pores between the EPS granules and the increase in stiffness and strength of the calcium silicate hydrate gels formed as a result of hydration caused an increase in the bending strength. As a result of the dispersion of the cement particle size, the spread of the hydration reactions over time causes the specimens to show continuity even if the strength gains rate decreases. In this study, it was observed that the bending strength of the 7 day specimens could reach up to 93% of the bending strength of the 28 day specimens. In the case of the addition of plasticizer, the homogeneous distribution that occurs as a result of preventing the flocculation of the cement grains provided better placement in the cross-section, and in this case, the bending strength of the specimens increased by up to 24%. In the studies conducted by Jayanth and Sowmya (2018), it was determined that the flexural strength of epscrete specimens decreased to 0.98 MPa.

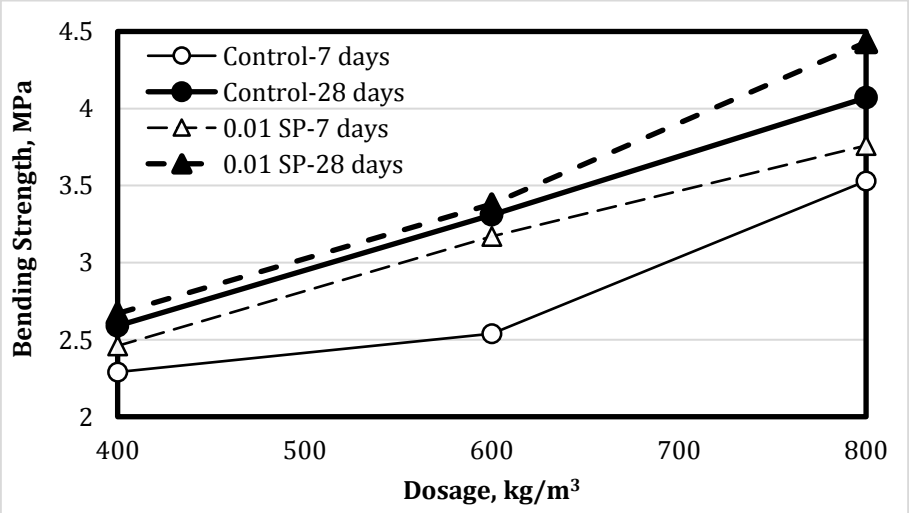

Fig. 6. Effect of dosage on bending strength of epscrete.

The variation in compressive strength of epscrete specimens depending on admixture content, specimen age, and cement amount is shown in Fig. 7. It was observed that the compressive strengths of the specimens varied between 8.5 and 19 MPa. The compressive strengths increased up to 82%, depending on the amount of cement used. In case of an increase in dosage, an increase in strength is an expected situation. However, the use of EPS grains as aggregate in epscrete specimens and the fact that these grains act as voids and do not contribute to strength, it has been observed that the contribution of cement paste to strength is effective. In normal concrete, the 7 day concrete compressive strength is 70% of the 28 day concrete compressive strength. The 7 day compressive strength of Epscrete specimens was at least 76% of their 28 day compressive strength. The plasticizer admixture separated the cement particles from each other by physical force, preventing segregation and increasing the compressive strength. This increase reached 20% in epscrete specimens. When the studies conducted by Kuhail (2001), Jayanth and Sowmya (2018) are examined, the compressive strength of epscrete samples using 400 doses of cement decreases to 4.5 MPa, while the compressive strength can reach up to 6 MPa in case of using 600 doses of cement.

SEM images of epscrete produced by using EPS beads as aggregate are given in Fig. 8. When Fig. 8 is examined, porous structure of the EPS beads and the microstructure of the interface formed by the bonding of EPS to the cement paste are seen.

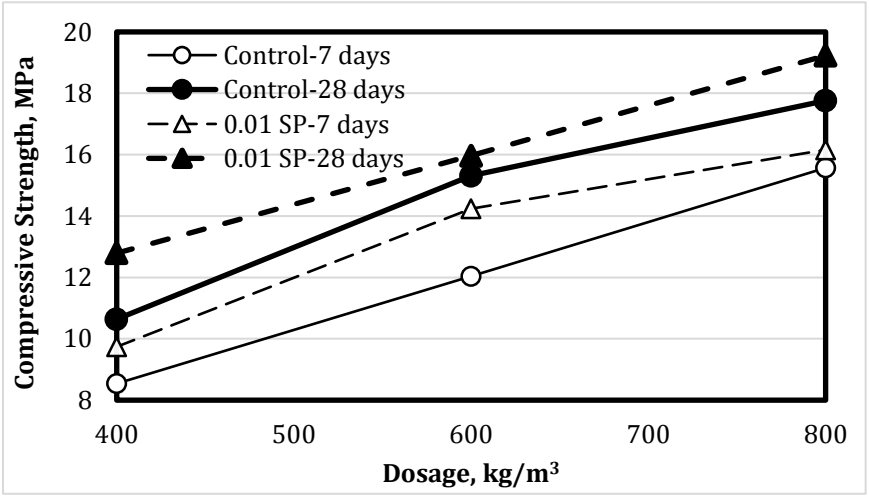

Fig. 7. Compressive strength variation of epscrete with dosage.

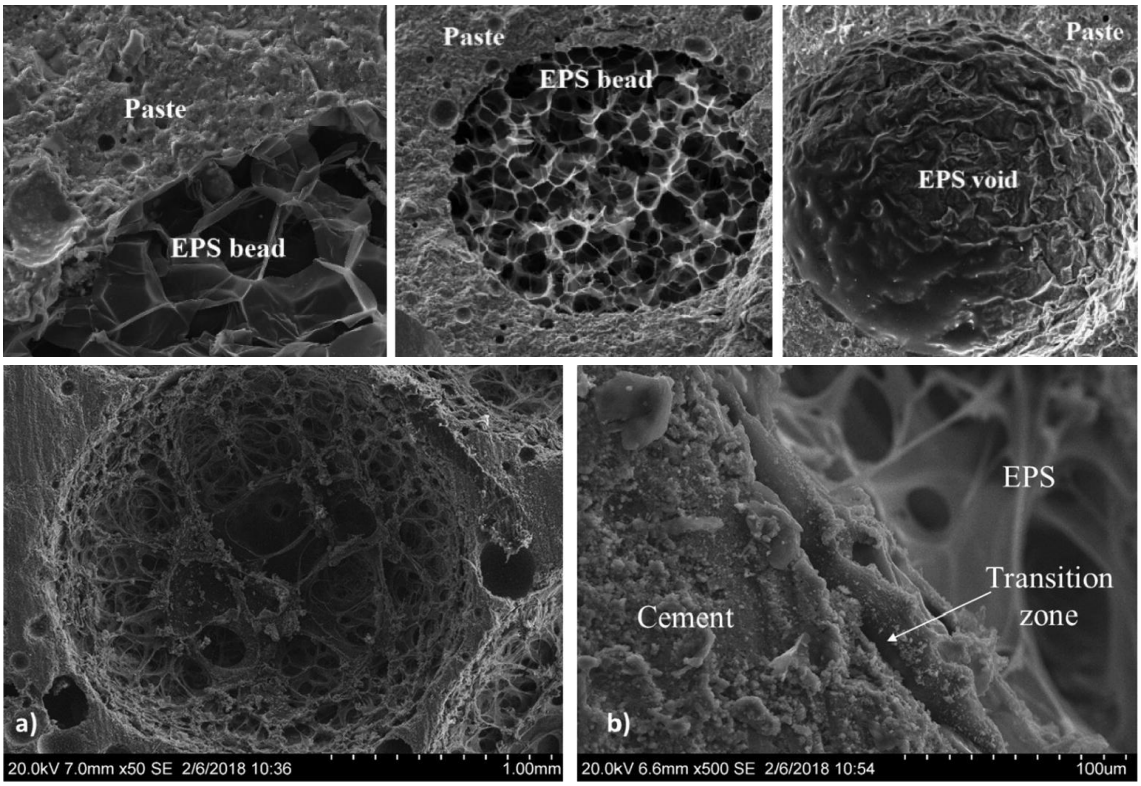

Fig. 8. SEM images of the cement paste/EPS interface and EPS beads (Allahverdi et al. 2018; Maaroufi et al. 2018).

4. Conclusions

The following conclusions were reached as a result of the tests and analysis on epscrete.

- It has been observed that the amount of cement selected such as 400, 600 or 800 kg in epscrete production has a significant effect on the test results to determine the mechanical and physical properties.
- It was observed that the unit weights of 400 dosage epscrete fell below 700 kg/m^3. It was determined that the unit weights of the specimens with 800 dosages were over 1200 kg/m^3.
- As a result of the decrease in space contained in the specimens and the increase in dosage, the ultrasonic pulse velocity values increased while the water absorption rates decreased.
- Considering the compressive and bending strengths, which are the most important mechanical properties of concrete elements, the dosage increase increased the strengths. While the bending strengths of 400 dosage specimens were 2.6 MPa and the compressive strengths were around 11 MPa, the bending strengths of 800 dosage specimens were around 4.1 MPa and the compressive strengths were around 18 MPa.
- The workability of the mixture has increased with the addition of plasticizer to the epscrete mixture. This situation caused an increase in the unit weight, ultrasonic pulse velocity values, bending and compressive strengths of the specimens and a decrease in the water absorption rate. Especially in 400 dosage epscrete specimens, the compressive strengths reached 13 MPa.
- The physical and mechanical properties of epscrete specimens at 7 and 28 days were determined. While the ultrasonic pulse velocity values and compressive and bending strengths of the 7 day specimens are lower than those of the 28 day specimens, their unit weights are high.
- While 87% of the bending strength was reached in terms of mechanical properties at an early age, 80% of the compressive strength was reached in 400 dosage specimens and 87% in 800 dosage specimens. High strength achieved at an early age was one of the important results of this study.

Epscrete specimens with 800 dosages are suitable to be produced as a partition wall block construction element with their 1.2 kg/dm^3 unit weight and 18 MPa compressive strength. The mechanical properties obtained show that these blocks are suitable for use as lightweight load-bearing wall elements in masonry structures. When 400 dosages are preferred in epscrete production, it is recommended to use the products obtained as an insulation plate with unit weights of 0.6 kg/dm^3, bending strengths of 2.6 MPa and compressive strengths exceeding 10 MPa. However, in order to be used as an insulation plate, it is recommended to determine the thermal conductivity coefficients in future studies.

Acknowledgements

None declared.

Funding

The authors received no financial support for the research, authorship, and/or publication of this manuscript.

Conflict of Interest

The authors declared no potential conflicts of interest with respect to the research, authorship, and/or publication of this manuscript.

References

Allahverdi A, Azimi A, Alibabaie M (2018). Development of multi-strength grade green lightweight reactive powder concrete using expanded polystyrene beads. *Construction and Building Materials*, 172, 457-467.

Assaad J, Mikhael C, Hanna R (2022). Recycling of waste expanded polystyrene concrete in lightweight sandwich panels and structural applications. *Cleaner Materials*, 4, 100095.

Babu DS, Ganesh Babu K, Tiong, Huan W (2006). Effect of polystyrene aggregate size on strength and moisture migration characteristics of lightweight concrete. *Cement and Concrete Composites*, 28(6), 520–527.

Feng X, Gong B, Zhao T (2022). Study on the non-linear deformation and failure characteristics of EPS concrete based on CT-scanned structure modelling and cloud computing. *Engineering Fracture Mechanics*, 261, 108214.

Gyawali R (2023). Effect of the mixing procedure on the properties of lightweight EPS mortar. *Journal of Building Engineering*, 68, 106012.

Jayanth P, Sowmya M (2018). Experimental Study on replacement of coarse aggregates by EPS beads in concrete to achieve lightweight concrete. *International Research Journal of Engineering and Technology*, 5(7), 610-616.

Jiang T, Wang Y, Shi S, Yuan N, Ma R, Wu X, Shi D, Sun K, Zhao Y, Li W, Yu J (2022). Compressive behavior of lightweight concrete using aerogel-reinforced expanded polystyrene foams. *Case Studies in Construction Materials*, 17, e01557.

Kuhail Z (2001). Polystyrene Lightweight Concrete (Polyconcrete). *An-Najah University Journal for Research - A (Natural Sciences)*, 41–61.

Li C, Miao L, You Q, Hu S, Fang H (2018). Effects of viscosity modifying admixture (VMA) on workability and compressive strength of structural EPS concrete. *Construction and Building Materials*, 175, 342–350.

Maaroufi M, Abahri K, El Hachem C, Belarbi R (2018). Characterization of EPS lightweight concrete microstructure by X-ray tomography with consideration of thermal variations. *Construction and Building Materials*, 178, 339-348.

Maghfouri M, Alimohammadi V, Gupta R, Saberian M, Azarsa P, Hashem, M, Asadi I, Roychand R (2022). Drying shrinkage properties of expanded polystyrene (EPS) lightweight aggregate concrete: A review. *Case Studies in Construction Materials*, 16, e00919.

Mahmoud A, Tawfik A, Abd El-razik M, Faried S (2023). Mechanical and acoustic absorption properties of lightweight fly ash/slag-based geopolymer concrete with various aggregates. *Ceramics International*.

Meddage P, Chadee A, Jayasinghe R, Rathnayake U (2022). Exploring the applicability of expanded polystyrene (EPS) based concrete panels as roof slab insulation in the tropics. *Case Studies in Construction Materials*, 17, e01361.

Miled K, Le Roy R, Sab K, Boulay C (2004). Compressive behavior of an idealized EPS lightweight concrete: size effects and failure mode. *Mechanics of Materials*, 36(11), 1031–1046.

Mishra S, Dashore S. (2020). Analysis of fiber reinforced concrete with EPS. *International Research Journal of Engineering and Technology*, 7(2), 1875-1877.

Mohammed HJ, Zain M (2016). Experimental application of EPS concrete in the new prototype design of the concrete barrier. *Construction and Building Materials*, 124, 312–342.

Prasittisopin L, Termkhajornkit P, Ki H (2022). Review of concrete with expanded polystyrene (EPS): Performance and environmental aspects. *Journal of Cleaner Production*, 366, 132919.

Rauf MA, Shah A, Qazi EH, Tahir M (2011). Evaluation of expanded polystyrene based blocks for lightweight structures in the seismic prone areas. *International Conference on Earthquake Engineering and Seismology* (ICEES 2011), NUST, Islamabad, Pakistan.

Rosca B, Serbanoiu A (2022). Study on influence of natural aggregate maximum size on compressive strength of polystyrene aggregate concrete of structural grade. *Materials Today: Proceedings*, 61, 433-439.

Sadrmomtazi A, Sobhani J, Mirgozar A, Najimi M (2012). Properties of multi-strength grade EPS concrete containing silica fume and rice husk ash. *Construction and Building Materials*, 35, 211–219.

Susilorini R, Widianto D, Ogur I, Prabandaru S (2020). Flexural deformation of expanded polystyrene concrete sandwich beam: An experimental study. *International Journal of Engineering Research and Technology*, 13, 540-7.

Tang C, Lo Y, Nadeem A (2008). Mechanical and drying shrinkage properties of structural-graded polystyrene aggregate concrete. *Cement and Concrete Composites*, 30(5), 403–409.

Uygunoğlu T, Güneş İ, Çalış M, Özgüven S (2015). Investigation of behavior of EPS and XPS thermal insulation exterior claddings during fire. *Journal of Polytechnic*, 18(1), 21-28.

Vinod R, Surendra J, Shobha R (2022). Lightweight concrete blocks produced using expanded polystyrene and foaming agent. *Materials Today: Proceedings*, 52, 1666-1670.

Xiang J, Song Y, Shu H, Li Z, Qiu J, Gu X (2022). Expanded polystyrene (EPS) particles as a carrier to improve the growth of microorganisms in concrete. *Journal of Cleaner Production*, 369, 133363.

Yuan J, Li D, Li W, Yang H, Zhang W, Wang L, Wang J, Xiong Z (2022). Study on frost resistance of EPS concrete based on EPS beads wrapping modification. *Construction and Building Materials*, 345, 128400.

Challenge Journal of Structural Mechanics

Research Article

Potential improvement of clinker sand in the mechanical high temperature and transport properties with GGBS-based prepacked geopolymer composite

Haluk Görkem Alcan [a,*], Bilge Aksu Alcan [a], Barış Bayrak [a], Abdulkadir Cüneyt Aydın [b]

[a] *Department of Civil Engineering, Kafkas University, 36100 Kars, Türkiye*
[b] *Department of Civil Engineering, Atatürk University, 25240 Erzurum, Türkiye*

ABSTRACT

In this study, a new generation prepacked geopolymer composite (PGC) material that can meet different needs was obtained by combining geopolymer concrete (GPC) and prepacked aggregate concrete (PAC) technology. In the production of PGC, 5-8 mm quartz aggregates were placed in molds and, geopolymer mortar was injected between these aggregates. Aluminosilicate based blast furnace slag (GBFS) was used as binding in geopolymer mortars; sodium silicate (Na_2SiO_3) and sodium hydroxide (NaOH) was used as alkali activator. In addition, clinker aggregate in different proportions was used as fine aggregate (0–4 mm) in the production of mortar. Within the scope of the study, the physical, mechanical, permeability and high temperature resistance properties of PGC were investigated. The produced samples were cured at 30 and 60 °C for 6 and 8 hours. Hardened unit weights of PGC vary between 2342 and 2539 kg/m^3, and sorptivity values vary between 0 and 0.04 kg/m^2.min$^{0.5}$. While the increase in curing temperature and curing time increases the hardened unit weight values, it decreased permeability values. While the increase of clinker aggregate in the mortar phase does not change the hardened unit weight, it significantly reduced permeability. When the PGC samples are cured at 30 °C, the compressive strengths are 20.38–39.03 MPa; when curing at 60 °C, the compressive strengths are 35.21–57.04 MPa. Flexural strengths, 2.35–6.96 MPa with 30 °C cure, achieved 4.27–9.93 MPa results with 60 °C curing. Increasing the curing time and curing temperature significantly increased the compressive and flexural strengths. The increase in the amount of clinker aggregate added to the mortar phase decreased the strength values. While the compressive strength values of PGC mixtures do not fall below 15 MPa after being exposed to 300 °C high temperature; after the application of 600 °C high temperature, it lost up to 70% of its strength. Increasing the curing time and curing temperature, increased the high temperature resistance. The increase in the amount of clinker aggregate in the mixtures, decreased the strength loss rate.

ARTICLE INFO

Article history:
Received 21 April 2023
Revised 19 June 2023
Accepted 10 July 2023

Keywords:
Clinker aggregate
Composite material
Geopolymer concrete
High temperature
Mechanical properties
Prepacked aggregate concrete

1. Introduction

Ordinary Portland cement has a plastic consistency at first as a result of mixing cement, aggregate and water and, it gains strength and hardens over time (Aïtcin 2000). Concrete is one of the most preferred materials in construction systems, due to the reasons such as being able to give the desired shape in the fresh state, ease of transportation of its components and being economical (Khayat 1999; Meyer 2009). In addition to these advantages, it has been determined by previous studies that cement, which provides binding and strength to

* *Corresponding author*. Tel.: +90-474-225-1279 ; Fax: +90-474-225-1282 ; E-mail address: hgorkemalcan@kafkas.edu.tr (H. G. Alcan)
ISSN: 2149-8024 / DOI: https://doi.org/10.20528/cjsmec.2023.03.002

concrete, releases a high rate of CO_2 gas during the production process (Worrell et al. 2001; Barcelo et al. 2014). It is known that CO_2 emission is one of the main causes of global warming. It has been revealed that in the production of one ton of Portland cement (PC), almost 1 ton of CO_2 is released and, considering the "Mineral Raw Material Products Report" prepared by the US Geological Survey Department in 2023, around 4,1 billion tons of cement was produced in 2022 (Benhelal et al. 2013; Golewski 2021). The importance of the amount of CO_2 released to the atmosphere is clear. It has been revealed by scientists that, PC is responsible for about 10% of global CO_2 emissions (Suhendro 2014; Winnefeld et al. 2022). In order to eliminate the mentioned disadvantage, "geopolymer concrete" which is a more environmentally friendly and sustainable type of concrete, has been the focus of attention of researchers in recent years (Amran et al. 2021; Wasim et al. 2021). In the production of geopolymer concrete (GPC), inorganic materials such as blast furnace slag (GBFS) and fly ash (FA) are generally used as binders instead of cement used as binder in ordinary Portland cement (OPC). In addition, in recent years, different alumina silicate-based inorganic materials such as silica fume, rice husk ash, metakaolin and volcanic glasses have been used in the production of geopolymers (Ahmed et al. 2022; Jindal et al. 2022). The majority of these binders are obtained through the recycling of industrial wastes and approximately 80% less CO_2 is released into the atmosphere compared to Portland cement (PC) (van Deventer et al. 2010; Zhang et al. 2020). By activating the inorganic materials used in the production of GPC with alkalis such as sodium hydroxide (NaOH), sodium silicate ($nSiO_2Na_2O$), it gains binding property as a result of geopolymerization reactions. As a result of these reactions, N-A-S-H in amorphous structure and zeolite in $(NaAlO_2)_7(SiO_2)_9$ structure are formed (Khalid et al. 2019; Krishna et al. 2021). Geopolymer has advantages such as fast hardening, high compressive strength, high acid and fire resistance, low thermal conductivity, low shrinkage, depending on curing conditions and the raw material selection; as well as causing less environmental pollution and producing less energy. The mentioned properties of GPC depend on many factors such as type and content of inorganic material used, type of activator, amount and type of aggregate, curing temperature and curing time (Mohammed et al. 2021; Raza et al. 2022).

Prepacked aggregate concrete (PAC) is a particular type of concrete produced by injecting mortar or cement paste on it after the aggregates are placed in the mold with maximum compactness (Wakeley and Roy 1983). PAC can be preferred in cases where it is difficult to reach, difficult to make molds, and difficult to pour and compact the concrete. In addition, In addition, PAC is preferred in underwater concrete and repair works due to its low shrinkage and high impermeability (Cheng et al. 2019). The coarse aggregate volume in the PAC is around 65-70% and the remaining voids are filled with flowing mortar (de Castro and de Brito 2013). In this type of concrete, the aggregate mix has a discrete granulometry. Thus, it is ensured that coarse aggregated particles come into contact with one another and that there is enough space between the particles to be filled with dough or mortar. PAC contains more coarse aggregate than normal concrete. Therefore, especially the modulus of elasticity is higher than that of normal concrete, and the drying shrinkage is lower (Das et al. 2021). In PAC, the aggregates are in direct contact. That is, they are in grain-grain contact that can cause stress distribution throughout the aggregates (Domingo-Cabo et al. 2009). Since both the coarse aggregates are in contact and the injection paste or mortar completely fills the spaces between the aggregates, the permeability of the prepackaged concrete with a very low void ratio is also very low, and therefore, its resistance to freeze-thaw and chemical attacks is high. Another advantage is that when applied on old concrete in repair works, its adherence is quite good. This is because the fluid paste or mortar used effectively penetrates the voids of the previously roughened concrete surface (Lv et al. 2020). Due to the very low shrinkage of the Prepacked aggregate concrete, the stresses that will occur at the interface are minimized and an effective adhesion, is provided between the two concretes. In addition, in concretes that will act as a shield against nuclear radiation, PAC application in which heavy coarse aggregate and fine aggregate are placed separately, can be advantageous in order to prevent segregation (Yoon et al. 2020).

A variety of studies have been undertaken to examine the effects of concrete under high temperature. According to these studies, when the concrete reaches a temperature of 200 °C, the water in the cavities is removed from the cracks by evaporation. Thus, the water pressure in the concrete decreases, and as the expansion decreases and, the distance between the atoms becomes shorter. As a result, the compressive strength of the concrete increases somewhat as the water escapes (Noumowe 2005; Behnood and Ghandehari 2009). The temperature is above 400 degrees Celsius, as the $Ca(OH)_2$ structure begins to decompose, the cracks in the concrete increase and its strength decreases (Huo et al. 2009). As the temperature of the concrete exceeds 600 °C, the aggregates in it begin to expand. As a result of this expansion, cracks occur as parasitic stresses occur in the concrete. As the temperature and degree of exposure of the concrete increase, the compressive strength of the concrete decreases with the increase in the number and width of these cracks (Schneider 1988; Sukontasukkul et al. 2010). When the temperature reaches 1000 - 1200 °C, the dehydrated phases in the CSH structure which is the basic skeleton of concrete strength, deteriorate. After this temperature, the concrete loses its strength and loses its carrier property (Chan et al. 1999; Arioz 2009). Although studies have been conducted recently to examine the mechanical and durability properties of geopolymer concretes, research on high temperature resistance has been more limited. It has been found that GPC has a greater ability to resist microstructural damage exposure to elevated temperatures than conventional mortars and concrete. The pores of the GPC in the gel and matrix limit the transport of water vapor when exposed to high temperatures, so the high temperature resistance of geopolymer concrete is more stable than OPC (Aredes et al. 2015; Samal 2019). The size and connection form

of the pores in the internal structure of GPC are similar to those that determine its mechanical and durability properties (Gültekin et al. 2022).

Concrete is basically a composite construction material composed of aggregates and paste phase. When concrete is examined in the microstructure, it is known that apart from these two phases, it is an interfacial transition zone (ITZ) (Aydin et al. 2007). The pores, cracks and voids in the concrete are concentrated in the ITZ onto the aggregate surface. The formation of cracks due to stresses in the concrete under load spreads starting from here. The strength and durability properties of concrete are closely related to the interface region. Since the mechanical strength of ITZ is lower than that of aggregate and paste, researchers have extensively studied the behavior of this region. As a result of the researches, properties such as the diameter, roughness, mineral structure of the aggregate, both the water/cement ratio and the type of cement, affect the microstructure of ITZ (Prokopski and Halbiniak 2000; Aldanmaz 2020). The addition of inorganic pozzolans such as fly ash, silica fume and blast furnace slag to the concrete mix, not only contributes to the hydration reaction, but also enhances mechanical and durability properties of concrete decreasing the porosity of ITZ (Topçu and Canbaz 2008). Apart from this method mentioned, using active aggregate also provides positive contributions to the concrete (Beshr et al. 2003; Titi and Tabatabai 2018). Portland cement clinker has also been observed to be used as an active aggregate because of its hydrated formation properties in the presence of water. There are studies showing that when clinker is used as an alternative to natural aggregate, the compressive strength increases, chlorine permeability and diffusion coefficient decrease with the increase in the interfacial phase (ITZ) compaction (Berger 1974; Shafaghat and Allahverdi 2019).

In this study, prepacked geopolymer composite (PGC) was produced by using PC clinker instead of fine aggregate. By applying two different curing temperatures (30–60 °C) to PGC samples instead of the long curing time applied in the literature, a short curing time (6–8 hours), the effects of these parameters on physical, mechanical and permeability values were investigated. Another unique value of the study is the observation of the effect of different high temperature values (300 and 600 °C) on the mechanical strength of PGC.

2. Experimental Work

2.1. Materials

In this study, aluminosilicate-based granulated blast furnace slag (GBFS) used as inorganic binder, was obtained from a local company and it was chosen according to ASTM C989 (2006) standard. The average particle size (d_{50}) of GBFS used in the experiments is 30 μm, its specific weight is 2.78 gr/cm^3, and its specific surface area is 5090 cm^2/g. Sodium silicate (Na_2SiO_3) as well as sodium hydroxide (NaOH) solutions were used for blast furnace slag activation throughout the experiments. Both solutions are in liquid form and, while the specific gravity of Na_2SiO_3 is 1.66 gr/cm^3, it consists of approximately 64% water. NaOH is 99% pure with a solution molarity of 12M. While the specific gravity of NaOH is 1.61 gr/cm^3, 63.9% of the solution consists of water. The ratio between of sodium silicate and sodium hydroxide used in the study is 2.5. The solutions used, were prepared 24 hours before starting the experiments.

In producing PAG, clinker was used instead of fine aggregate with 0–4 mm sieve opening. Clinker was obtained from an OPC manufacturing plant and its specific gravity was 2.96 g/cm^3 and the water absorption rate was 0.5%. In addition, quartz (QA) in sizes (5–8 mm) described as coarse aggregate was used in the study. The specific gravity and water absorption of the quartz aggregate are 2.71 gr/cm^3 and 0.9%, respectively. The chemical and physical properties of GBFS and QA used throughout this study are presented in Table 1, and the XRD pattern of GBFS is presented in Fig. 1. In addition, the materials used during the experiments are shown in Fig. 2.

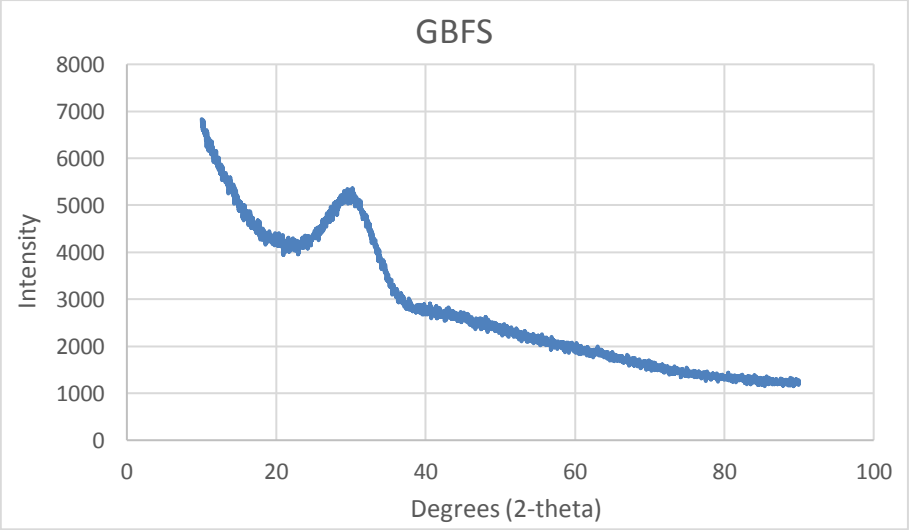

Fig. 1. XRD pattern of GBFS.

Table 1. Chemical, Physical properties of GBFS and QA.

	Oxide	CaO	SiO_2	Al_2O_3	Fe_2O_3	MgO	SO_3	LOI*	Specific gravity	Specific surface area
GBFS	%	34.4	37.7	11.4	5.3	6.88	0.8	0	2.96	5090**
QA	%	0.5	98.2	0.08	0.26	0.02	<0.01	0.67	2.71	-

*Loss on ignition; **Blaine method (cm^2/g).

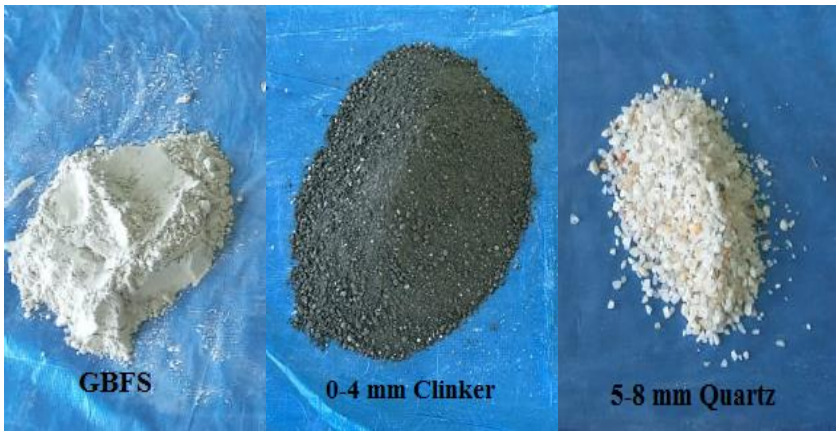

Fig. 2. Used materials in experiments.

2.2. Mixing, casting and curing

Production of PGC samples was done in a stepwise fashion. First, coarse aggregates (QA) were placed in the molds. The amount of QA in all mixtures is constant (800±5 kg/m³) and, this ratio constitutes approximately 45% of the volume of the mold. On the other hand, a 5 liter Hobart mixer was used to prepare geopolymer mortar. During mortar production, while the amount of GBFS and clinker aggregate varies according to the groups, the amount of NaOH and Na_2SiO_3 was kept constant in all groups. GBFS and 0–4 mm clinkers were first added to the mixer and mixed at low speed for 2 minutes. Then, liquid NaOH was added to the dry ingredients and mixed at low speed for another 2 minutes. Finally, liquid Na_2SiO_3 was added to the mixture and the mortar phase was obtained by mixing at high speed for another 5 minutes. In the production of the mixtures, no superplasticizer and water were added at any stage. While the mortar in the mixer was placed in molds filled with QA, vibration was applied to obtain a homogeneous mixture and to wrap the coarse aggregates in the mortar. The molds of the samples whose production has been completed are wrapped with plastic stretch. In this way, the evaporation of alkalis is prevented during thermal curing. The production process of PGC samples is presented in Fig. 3. Within the scope of this study, 8 different groups were produced and the mixing ratios are given in Table 2. Within the scope of this study, approximately 300 samples were produced depending on the variable experimental parameters.

After the PGC casting was completed, it was placed in the furnace for heat curing with a heating at 5 °C/min and presented in Fig. 4. The samples were subjected to a 6 or 8 hour heat cure at 30 and 60 °C. The samples which completed the curing period, were taken out of the furnace and cooled slowly at room temperature. After the cooled PGC mixtures were removed from their molds, physical and mechanical experiments were carried out.

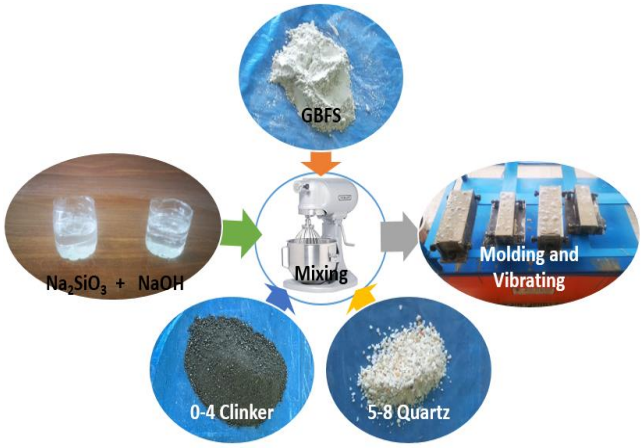

Fig. 3. PGC production process.

2.3. Tests

The hardened unit weights of the PGC samples were measured after heat curing. These were determined in 50×50×50 mm cube samples in accordance with the ASTM C642 (2006) standard based on the Archimedes principle. Capillary absorption of water calculation of PGC mixtures was made according to EN 1015-18 (2002). For these experiments, 50×50×50 mm cubes were produced and the sides of the specimens were covered with silicone. At the end of 24 hours, the amount of water absorbed through capillarity of samples was noted and necessary calculations were made. To determine the strength properties of PGC samples; after heat cure, the samples were three-point flexural test according to

ASTM C348 (2008) and compressive test according to ASTM C349 (2008). The dimensions of the samples produced for flexural strength are 40×40×160 mm, and the dimensions of those produced for compressive strength are 50×50×50 mm. In addition to the physical and mechanical tests applied in this study, the high-temperature resistance of PGC was also measured. The changes in the mechanical properties of the samples were determined after being exposed to high temperatures such as 300 and 600 °C. In the high temperature experiments, 50×50×50 mm cube samples were placed in a laboratory high temperature furnace (Fig. 5) with a heating rate of 10 °C/min. After keeping the PGC samples at the determined high temperature (300 and 600 °C) for 2 hours, they were left to cool at room conditions for 24 hours. As mentioned above, the cooling samples were subjected to compressive tests and their strength changes were measured. In all the experiments mentioned, three samples were tested and, their average values are presented for the accuracy of the results.

Table 2. PGC mixtures.

Mix (kg/m^3)	M1	M2	M3	M4	M5	M6	M7	M8
GBFS	850	800	750	700	650	600	550	500
Clinker (0–4 mm)	150	200	250	300	350	400	450	500
Quartz Ag. (5–8mm)	800	800	800	800	800	800	800	800
NaOH	160	160	160	160	160	160	160	160
Na_2SiO_3	400	400	400	400	400	400	400	400

Fig. 4. 30 °C and 60 °C heat curing of PGC samples.

Fig. 5. High temperature furnace.

3. Results and Discussion

3.1. Physical properties

In Fig. 6(a-b), the hardened unit weights observed after curing the GPC blends at 30 and 60 °C respectively are given. After the measurements, it was determined that the unit weights of the PGC samples were close ones between approximately 2342 and 2539 kg/m^3. This situation can be accepted as an indication that the aggregates are positioned in the mould and the mortar is poured homogeneously. Increasing the curing time from 6 hours to 8 hours at 30 and 60 °C slightly increased the hardened unit weight values. As GBFS grains become more activated later on, it can be interpreted that the chain-structured reaction products increase. It has also been observed that due to the fact that the curing times are close to each other, the results change less. Increasing the curing temperature from 30 °C to 60 °C, the hardened unit weight values increased significantly. This situation was interpreted as the formation of more gel products as a result of geopolymerization reactions. If the impact of curing temperature and curing time on hardened unit weight is examined, it was observed that the increase in curing temperature affected these values more. For example, while the hardened unit weight of the M1 mixture which was cured for 6 hours at 30 °C was 2352 kg/m^3, this value was measured as 2359.4 kg/m^3 by increasing the curing time to 8 hours at the same temperature. When the same M1 mixture was cured at 60 °C

for 6 hours, its unit weight reached 2443.2 kg/m^3. Since the same weight of clinker aggregate is added instead of GBFS removed from the mixture, the increase in the amount of clinker aggregate did not change the hardened unit weight much. In addition, the fact that the coarse aggregate and activators were constant in all mixtures was thought to be another reason for the formation of this result.

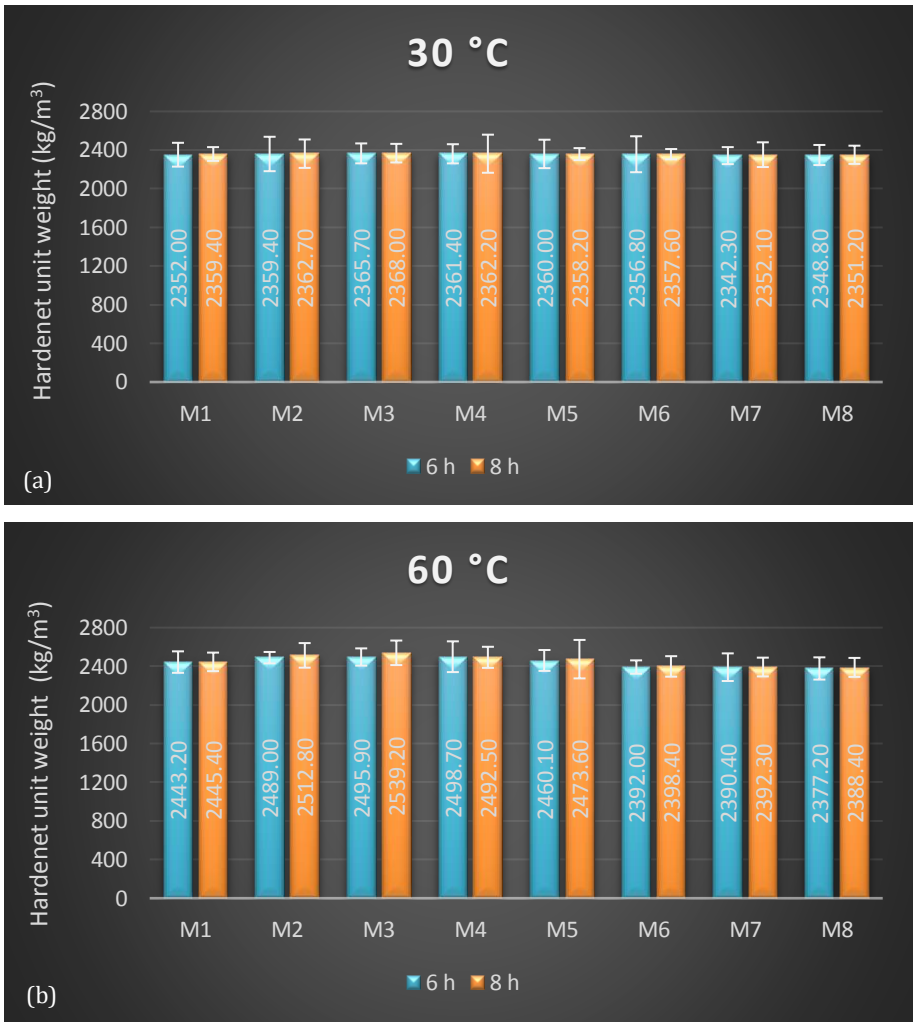

Fig. 6. Hardened unit weights of GPC: (a) 30 °C curing; (b) 60 °C curing.

Öz et al. (2022) added quartz sand in different proportions instead of natural sand to slag and metakaolin based geopolymer concretes. Three different curing times (6, 8 and 10 hours) and three different curing temperatures (40, 60 and 80 °C) were applied to the mixtures they produced. As a result of their measurements, they observed that the hardened unit weights were between 2160 and 2346 kg/m^3. They reported that the cured unit weights decreased with the increase of curing time and curing temperature. They interpreted this result as the evaporation of the activators with the effect of temperature and the lower unit weight of the added quartz aggregate compared to the natural sand. Durak (2022), cured the geopolymer mixture in which fly ash was used as a binder at 100, 200, 300, 400, 500, 600, 700 and 800 °C in 30 and 60 minutes. After a short curing of 30 minutes at 300 °C, satisfactory values like 9.8 MPa flexural and 32,8 MPa compressive strength were observed. In addition, it was emphasized that the cured unit weights of the mixtures decreased with the rise of the curing temperature and time. Albitar et al. (2017) produced geopolymer concrete in which fly ash was used as the precursor, and ordinary Portland cement samples. After exposing the mixtures to acid effect for 9 months, the hardened unit weight changes were examined. As a result of their study, the mass loss of OPC-based concrete was 11% higher than that of geopolymer concrete. They observed from the results that gel products formed as a result of geopolymerization reactions are more resistant to acids than CSH structures in concrete. In their study, Sevinç and Durgun (2020) produced geopolymer concrete by using fly ash, silica fume and glass powder materials in different proportions. They stated that both the fresh and hardened unit weights of the mixtures increased with the increase in the amount of glass powder used and the molarity of the activator. In their experiments, they observed that the hardened unit weight values were between 1920 and 2310 kg/m^3. They stated that the mechanical strength properties of the mixtures with higher hardened unit weights are generally good.

3.2. Mechanical properties

The compressive strength of PGC samples heat treated at 30 °C for 6 and 8 hours is shown in Fig. 7(a). The compressive strength of the samples which were heat cured at 60 °C for 6 and 8 hours, is presented in Fig. 7(b). In the study, the extension of the curing time generally contributed positively to the compressive strength. Extending the curing time indicates that the number of gel products formed in the microstructure increases more. In the groups in which the amount of clinker aggregate increased, the extension of the curing time had less effect on the strength. CSH structures released as a result of the hydration of clinker are formed more slowly than the chain Si-O-Al structures that form the skeleton of the geopolymer. Therefore, increasing the curing time from 6 hours to 8 hours did not affect the strength values much. This result indicates that if geopolymer mixtures are prepared using clinker aggregate, the curing time will be shortened and thus the energy spent for thermal curing will be reduced. In addition, this may be an indication that the clinker aggregate samples will continue to gain strength in advancing ages. Increasing the curing temperature had a positive effect on the strength of the PGC samples. While the compressive strength of the samples cured at 30 °C varies between 20.38 and 39.03 MPa, the compressive strength of the samples cured at 60 °C varies between 35.21 and 57.04 MPa. If the temperature increased from 30 °C to 60 °C, the compressive strength increased between 21% and 47%. This result indicates that the curing temperature of 30 °C is not suitable enough for mixtures. In other words, for the strength of the mortar phase, it can be interpreted that the products of geopolymerization develop better at 60 °C. Another interpretation is that the strength of the matrix surrounding the aggregates is important for the strength of the prepack concrete. In addition, it is seen that the compressive strength values decrease as the amount of clinker aggregate in the PGC mixture increases, that is, from the M1 mixture to M8. It has been explained in the above section that the increase in the amount of clinker aggregates in the mixtures is achieved by decreasing the amount of GFBS. It can be said that the reaction of clinker aggregates with alkali activators is more limited than GFBS which is the reason for the observation of these results. However, considering that this strength loss is at acceptable levels and that clinker aggregates are included in the geopolymerization reactions, it has been determined that this material can be used in the mixture.

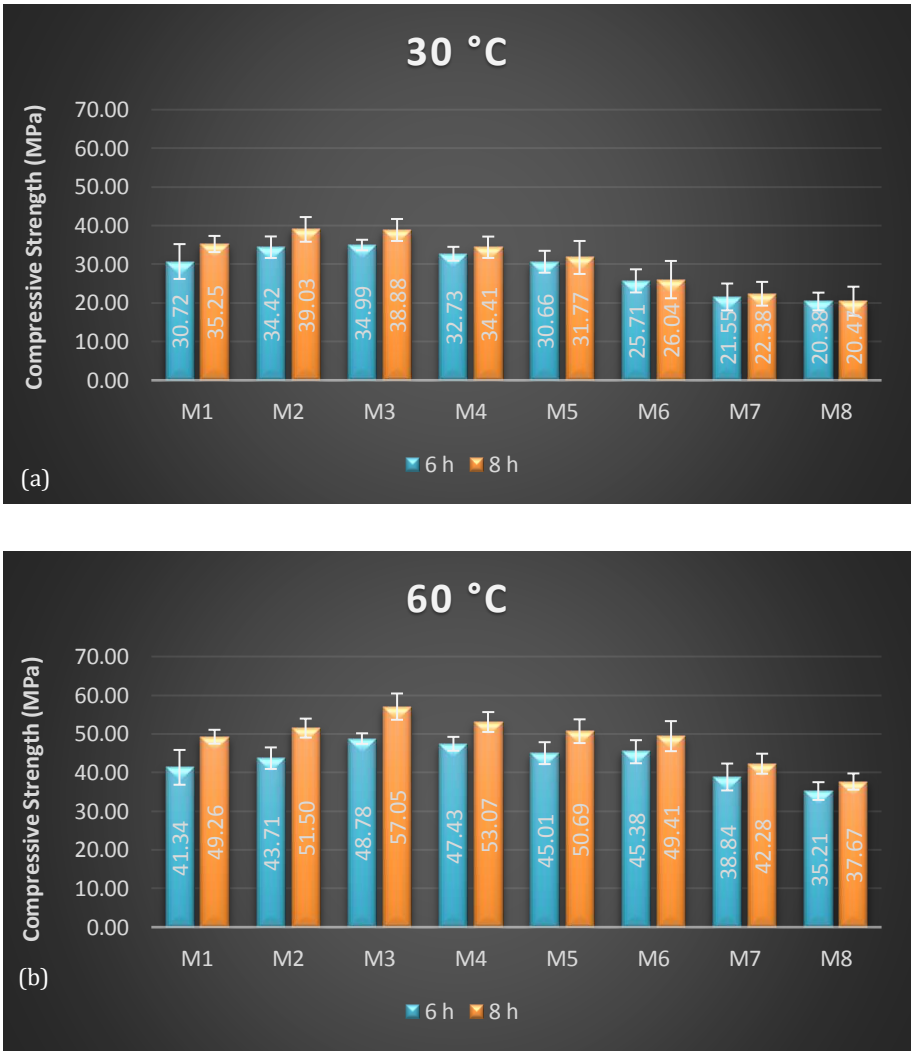

Fig. 7. Compressive strength of GPC: (a) 30 °C curing; (b) 60 °C curing.

Another remarkable result in Fig. 7 is that the compressive strength values increase as one goes from the M1 mixture to the M3 mixture for the whole curing temperature and curing time. When going from M3 to M8, it starts to decrease. The clinker aggregate added to M3 has increased the compaction of the mixture and an ideal aggregate-mortar ratio has been obtained for PGC. When going from M3 to M8 mixture, the strengths decreased by removing the amount of GFBS from the mixture at the rate that the clinker and aggregate increased and this ratio deteriorated. It has been interpreted that the amount of clinker aggregate added to the mixture is effective in the formation of these results.

In Fig. 8(a), the flexural strength results of the PGC samples are presented after curing at 30 °C, and in Fig. 8(b) at 60 °C for 6 and 8 hours. The flexural strength results generally showed parallelism with the compressive strength. As the curing time increases, the flexural strength of the samples increases with a greater rate up to the M4 mixture; after this group, the rate of increase remained at lower levels. The reason for this result is thought to be related to the gel products formed, the density and porous structure of these structures, as explained in the compressive strength. Increasing the curing temperature significantly increased the flexural strengths. While the strength values remained between 2.35–6.96 MPa at 30 °C, the strengths of the samples cured at 60°C reached results such as 4.27–9.93 MPa. Considering that this increase rate is between 20-88%, the role of curing temperature in the flexural strength of PGC samples can be better understood. As the temperature increased from 30 °C to 60 °C, the activity of GBFS grains increased, and it was thought that chain gel products were formed in greater quantity and in a shorter time. Another important finding obtained from the flexural strength result is the comparison of the compressive and flexural strength ratios of the PGC samples with the ratios in ordinary Portland cement. It is known that the ratio of compressive strength to flexural strength in ceramic materials such as concrete generally varies between 1/7 and 1/10. Based on this study and the information in the literature on Prepacked aggregate concrete, it has been observed that this ratio varies between 1/4 and 1/8. In ordinary Portland cement, the aggregates are usually in a discrete form, wrapped in the mortar phase without contacting each other. In addition, the amount of interfacial phase (ITZ) with a porous structure on the aggregate surfaces is high.

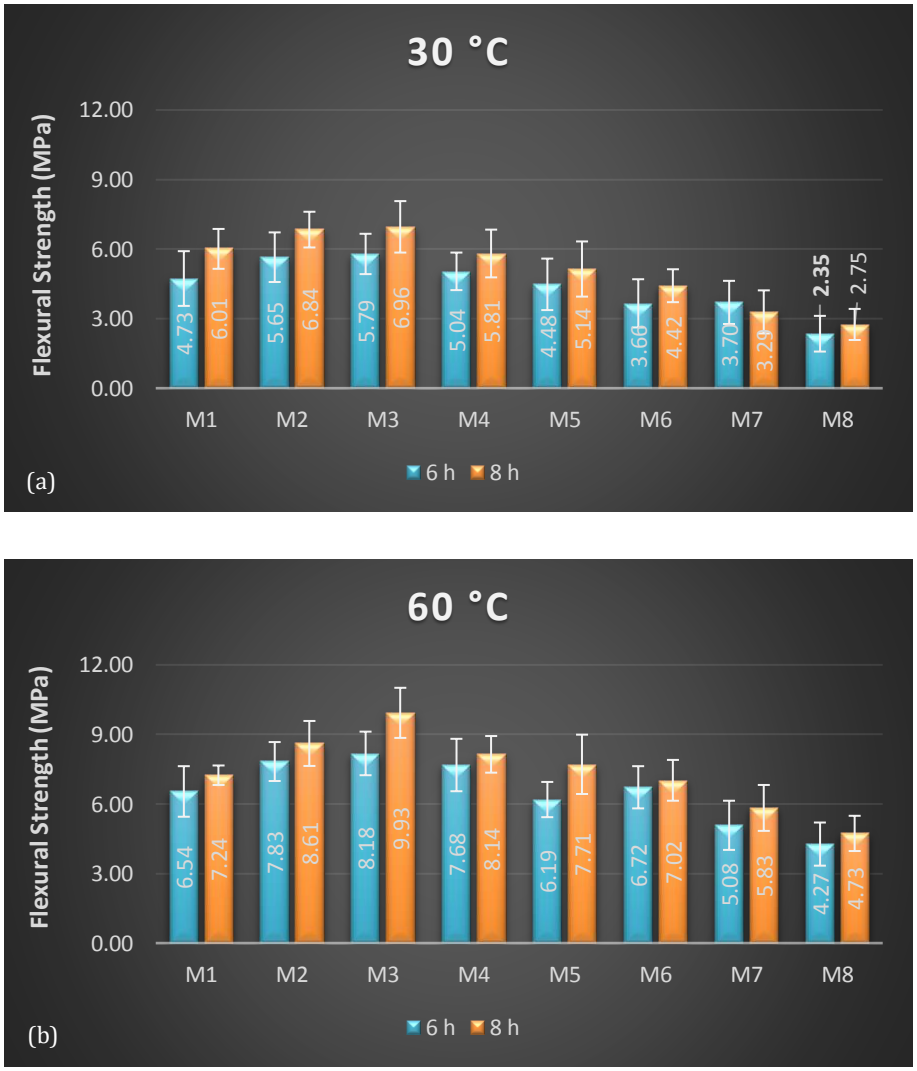

Fig. 8. Flexural strength of GPC: (a) 30 °C curing; (b) 60 °C curing.

In PAC, the amount of ITZ with voids is less than in ordinary Portland cement, because the aggregates with high rigidity come into contact with each other. For this reason, it is known that the flexural strength of prepacked aggregate concrete is relatively higher than that of ordinary Portland cement. The results obtained in this study were similar to this information. Based on this result, in productions where flexural strength is more critical, Prepacked geopolymer composite technology can be a solution. When the test data are examined, another observed result is that the flexural strength decreases somewhat as the amount of clinker aggregate increases. It has been interpreted that the reason for this decrease in flexural strength is similar to the reasons in compressive strength, that is, it is related to the amount of gel product formed in the internal structure. When the results of flexural strengths are examined, it is seen that the strengths increase from M1 to M3 and then begin to decrease under different curing temperatures and curing times. The reason for this situation is due to the aggregate-mortar ratio, as explained in the compressive strength results.

Güzelküçük and Demir (2019) investigated the compressive strength of perlite-based geopolymer concretes depending on the curing time and temperature. According to their results, they emphasized that the highest compressive strength was 46.76 MPa at 110 ºC curing temperature, 24 hours curing time. Hassan et al. (2019) investigated the change of the mechanical properties of geopolymer concretes, in which fly ash was used as binder, depending on the curing temperature. They stated that after applying ambient curing and 70 ºC temperature curing to the mixtures they produced, temperature curing improved the elastic modulus and other mechanical properties of geopolymer concretes. Kaplan et al. (2023) investigated the mechanical properties of Prepacked geopolymer concrete (PAG) mixtures. They reported that, PAG has approximately 70 MPa compressive strength and 5.5 MPa flexural strength values due to its high aggregate content. Verma and Dev (2022), investigated the mechanical strength and microstructure properties of blast furnace slag and fly ash based geopolymer mixtures depending on the curing temperature. According to the data they obtained, with the increase of curing temperature, the mechanical properties of geopolymer concrete such as compression, flexural and splitting tensile increased as well as its internal structure properties. Zhang et al. (2021) searched the mechanical properties of geopolymer concretes, in which they used metakaolin and silane at different dosages, according to different curing times. The geopolymer mixtures they produced were cured at room conditions for 28, 56, 90, 180 and 360 days. As a result of their experiments, the curing of the samples until the 90th day increases the compressive flexural strength; they observed that the strength values did not increase after this period. In their study, they measured the highest compressive strength and flexural strength of 51.4 MPa and 12.93 MPa, respectively, in the mixtures containing 1% by weight silane. Bing-hui et al. (2014) applied different curing temperatures and curing times in order to achieve the highest mechanical strength values of geopolymer concretes, in which metakaolin is used as a binder. They reported that the best compressive strength results were measured in groups cured at 97.95 MPa at 60 °C for 7 days. They stated that increasing the curing temperature and curing time increased the geopolymerization reactions.

3.3. High temperature effect

The measured compressive strengths of PGC samples cured at 30 °C after 300 and 600 °C high temperature application are shown in Fig. 9(a-b); The strength values of the samples cured at 60 °C after the same high temperature effect are shown in Fig. 10(a-b). When Figs. 9 and 10 are examined, the compressive strength of the PGC samples decreased compared to Fig. 7 after both high temperature applications. For example, while the compressive value of the M3 mixture cured for 8 hours at 60 °C which is not exposed to high temperatures, is approximately 57 MPa; after applying a temperature of 300 °C and 600 °C, its strength decreases by 56% and 70%, respectively. The products formed in geopolymer concretes to which GBFS is the binder are NASH and CASH gels. When the temperature is approximately 300 °C, the water in the gel structures starts to evaporate away from the hydroxyl structures. The expansion of the vapors formed and the movement of this steam cause the formation of microcracks in the internal structure. If the duration or degree of temperature is increased, the cracks formed begin to grow. In addition, since the increased temperature values greatly deteriorate the chemical structure of the gel products that make up the skeleton of the mixture, the strength of the specimens decreases. When the results are examined, the compressive strength values of the PGC samples can reach more than 15 MPa after processing at 300 °C; It lost up to 70% strength from the process at 600 °C. These results support the comments made. Another result from this is that the gel structure, which provides resistance at 300 °C, has begun to break down. Dehydration dimensions increased as the temperature reached 600 °C. These decreases in strength values showed changes according to the curing temperature, curing time and the amount of clinker aggregate in the mixtures. When the effect of curing temperature on high temperature resistance is examined, the application of high temperatures (300 and 600 °C) to PGC specimens cured at 30 °C decreased the strength values less than those cured at 60 °C. The lower compressive strength loss of the samples cured at 30 °C was thought to be related to the pozzolanic activity. In these groups, because the pozzolanic activity due to geopolymerization reactions is not completed at low curing temperatures, the gel products continued to form up to a certain temperature value. In PGC mixtures cured at 60 °C, it can be interpreted that almost all of the reaction products are formed. In addition, it was thought that the capillary void content was less in the mixtures cured at 60 °C, and therefore the evaporating water created more vapor pressure and damaged the internal structure. While the compressive strength of PGC mixtures cured at 30 °C varies between 15.21 and 23.35 MPa, the compressive strength of GPC mixtures cured at 60 °C was measured between 17.04 and 25.17 MPa. When the ef-

fect of curing time on high temperature resistance is examined, the strength of the samples with longer curing time after high temperature was higher than the samples with shorter curing time. It was observed that the compressive strength of PGC samples cured for 6 hours changed between 13.02–20.12 MPa after high temperature, and the samples cured for 8 hours changed between 12.53–25.17 MPa. The longer the curing time, the better the high temperature post-temperature resistance of the samples with longer curing time, as more geopolymerization reactions take place and accordingly more gel products are formed. The data obtained as a result of the experiments show parallelism with the comments. If the effect of the amount of clinker aggregate in the mixture on the high temperature resistance is examined, when Figs. 9 and 10 are examined, the strength loss rate of the samples decreased with the increase in the amount of clinker aggregate. For example, M1 mixture containing 150 kg/m^3 of clinker aggregate, cured at 60 °C for 8 hours, is 57% at 300 °C; at 600 °C, it lost 69% of its strength. In the M8 mixture containing the highest amount of clinker aggregate (500 kg/m^3), these rates were around 52% and 62%, respectively. It has been explained in the previous section with the reasons why the increase in the amount of clinker aggregate decreases the compressive strength. However, when the results of compressive strengths after the effect of high temperature are examined, increasing the amount of clinker aggregate decreased the strength loss rate. The structures of clinker aggregates are more porous than GBFS, therefore, mixtures with clinker aggregates have become porous. As the amount of clinker increased, the porosity ratio in the indirectly produced mixtures increased. Having more pores means creating more capillary spaces in the mixture. The water vapor formed in the internal structure of the PGC mixtures due to the effect of high temperature leaves the sample by advancing in the capillary spaces without damaging the matrix. However, it is known that the clinker aggregate has a $CaCO_3$ structure and this structure is dehydrated at high temperatures such as 900 °C. It should not be overlooked that this may be another reason why PGC samples with clinker aggregates experience less strength loss after high temperature.

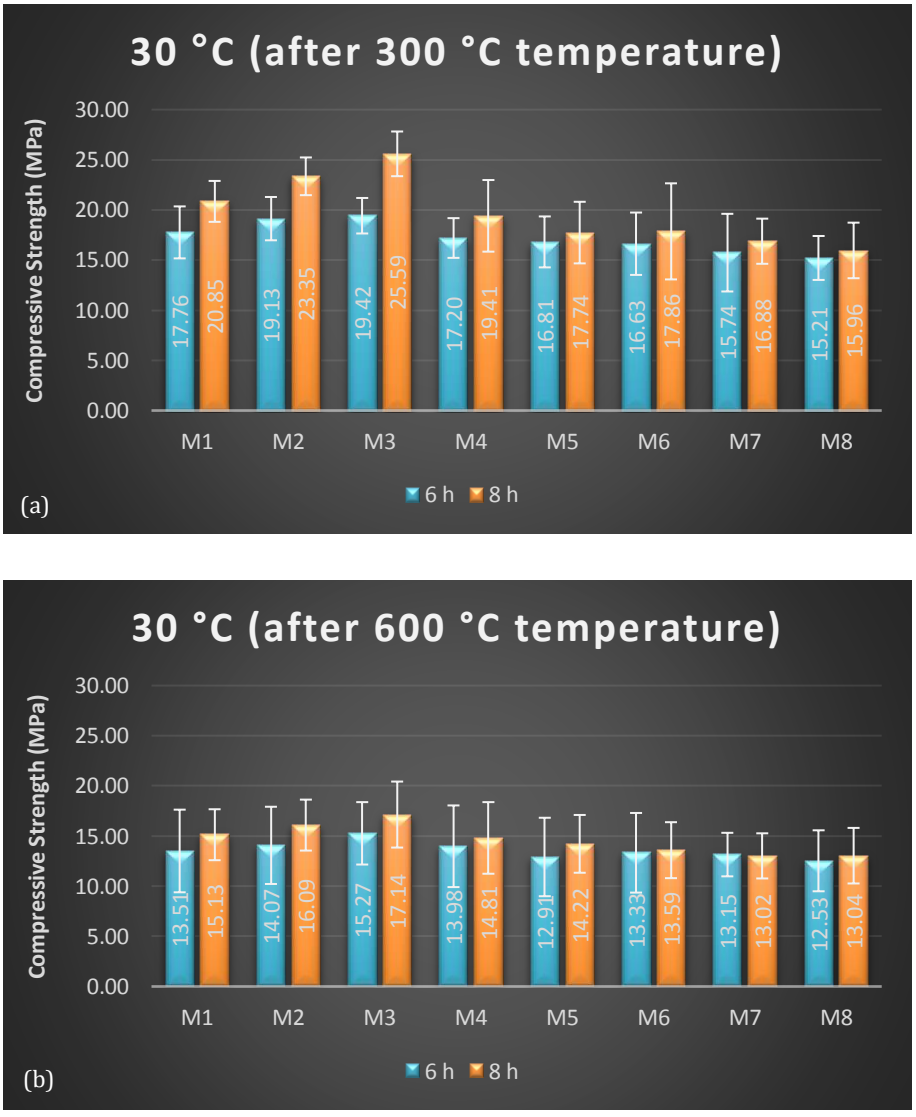

Fig. 9. Compressive strengths of PGC samples cured at 30 °C: (a) after 300 °C; (b) after 600 °C.

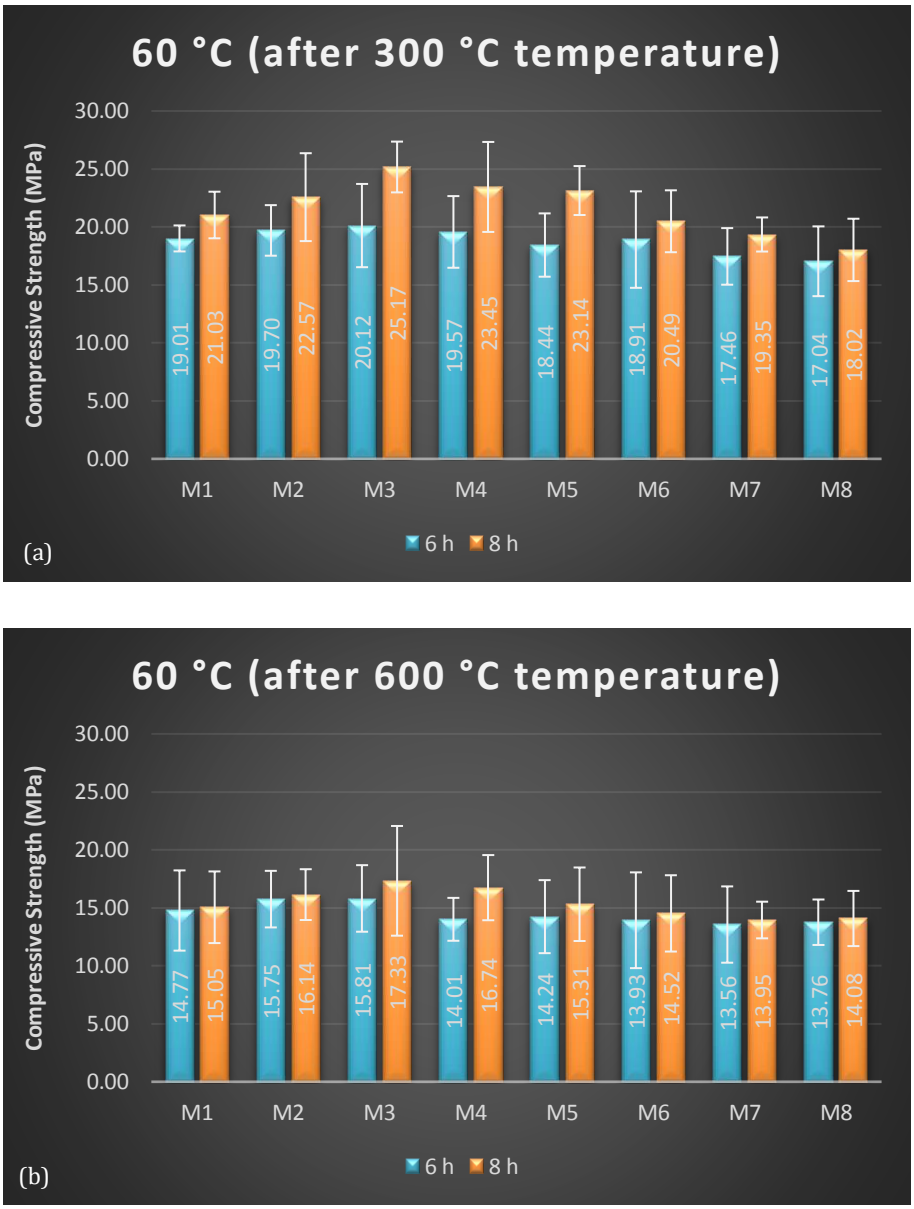

Fig. 10. Compressive strengths of PGC samples cured at 60 °C: (a) after 300 °C; (b) after 600 °C.

Nuaklong et al. (2021) used 25% and 50% by weight waste granite instead of river sand in the geopolymer mixture in their study. High temperature resistance was investigated by including fine aggregates in the mixture as saturated surface dry (SSD), air-dry (AD) and oven-dry (OD). As a result of their experiments, they determined that the waste granite geopolymer concrete showed a spalling behavior similar to that made from completely natural sand. In addition, they stated that due to the formation of capillary voids in the structure of dried aggregates, less strength loss was observed in these mixtures after high temperature. Tayeh et al. (2021) have produced lightweight geopolymer concrete in which fly ash and blast furnace slag are precursors. They investigated the mechanical behavior of these mixtures after high temperature using natural pumice and lightweight expanded clay aggregates in their mixtures. As a result of their experiments, they observed that the aggregates they used exhibited less strength loss than the mixtures using dolomite aggregate. They emphasized that the formation of this result is due to the hollow structures of natural pumice and expanded clay. Hager et al. (2021) applied high temperature up to 1000 °C to the geopolymer mortar samples they produced by adding blast furnace slag in different weight ratios instead of fly ash. They observed that with the temperature reaching 200 °C, the compressive strength increased by 30% and the flexural strength doubled. They determined that the strength values due to the deterioration of the internal structure decreased to 90% when the temperature reached 1000 °C. Kürklü, (2016) investigated the high temperature resistance of geopolymer concretes cured at 60 °C for 5, 24, 48 and 168 hours. After his experiments, he observed the highest flexural strength for 5 hours and the highest compressive strength for the mixtures cured for 48 hours. He also stated that 400 °C and 600 °C are critical temperatures for changes in mechanical and physical properties. He noted that with the final temperature value reaching 1000 °C, the strength values dropped significantly. Jaarsveld et al. (2002) investi-

gated the high temperature resistance of fly ash and metakaolin based geopolymer concretes. As a result of their experiments, they determined that the strength of the mixtures exposed to high temperature is closely related to the expansion temperature of the aggregate used. In addition, they emphasized that curing time and curing temperature are other important parameters for the high temperature resistance of geopolymer concretes.

3.4. Sorptivity

Sorptivity is based on the principle of measuring the water penetrating through the voids and cracks in the hardened concrete at certain time intervals. This value can guide the estimation of properties of concrete such as strength, durability and life of concrete. Sorptivity values are presented in Eq. (1). In this equation: C=Capillary water absorption coefficient (kg/m^2.min$^{0.5}$), M1= specimen mass after the immersion for 10 min (kg), M2=specimen mass after the immersion for 24 hours (kg).

$$C = 0.1 \cdot (M_2\text{-}M_1)\ \text{kg}/(\text{m}^2 \cdot (\text{min})^{0,5}) \quad (1)$$

It is calculated by the capillary water absorption coefficient. In Fig. 11 (a-b), capillary absorption of water values of PGC mixtures are presented. When the graphs are examined, the first striking result is that the capillary absorption decreases significantly with increasing curing temperature. Increasing the curing temperature from 30 °C to 60 °C caused the permeability values of the PGC samples to decrease by up to 50%. Increasing the curing temperature increased the geopolymerization degree of the mixture, resulting in more reaction products. Thus, a denser PGC microstructure was obtained, in other words, the porosity was reduced. As the curing temperature increased, the complexity of the matrix phase increased, which was interpreted as a decrease in capillary water absorption measured in the samples. Another remarkable result in Fig. 11 is that the permeability values decrease significantly with the increase of the curing time. The capillary water absorption results of the samples that were heat cured for 8 hours decreased between 15 and 35% compared to the samples cured for 6 hours. While the permeability values of PGC samples cured for 6 hours reached up to 0.04 kg/m^2.min$^{0.5}$; It was measured as 0.022 kg/m^2.min^{0,5} at most in the samples that were cured for 8 hours.

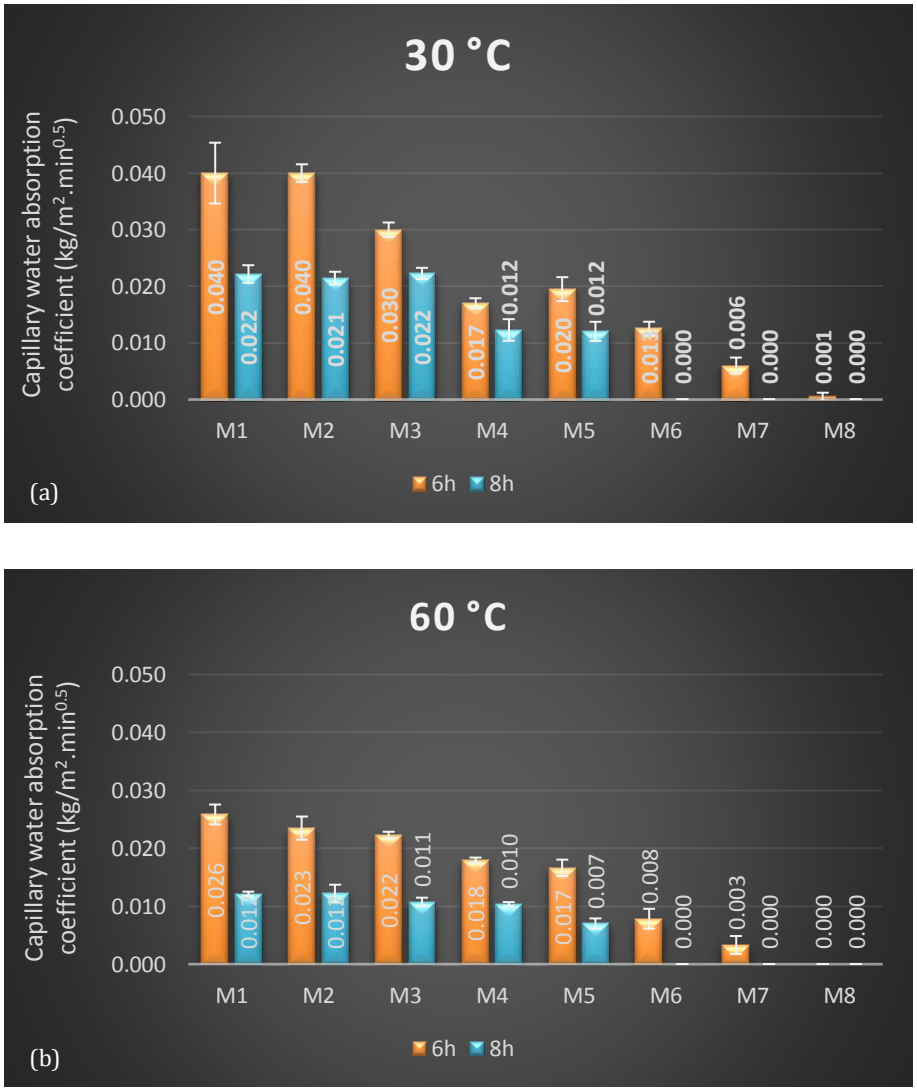

Fig. 11. Capillary water absorption coefficient of GPC: (a) 30 °C curing; (b) 60 °C curing.

It was thought that prolonging the curing time reduced the void ratio in the microstructure of the mixtures, creating more gel products. While examining the compressive and flexural strengths, it was mentioned in the previous section that the extension of the curing time increases the strength values. From this point of view, it is seen that the permeability results are compatible with the mechanical properties. Considering Fig. 11, a final observed result is that the permeability decreases as the amount of clinker aggregate in the mix increases. In fact, increasing the amount of clinker aggregate appears to be the parameter that decreases the capillary water absorption value the most. For example, permeability results in M8 mixture cured at different curing temperatures and times, it is measured as 0 $kg/m^2.min^{0.5}$. Clinker consists of calcium and silicate structures since its aggregates are obtained from OPC. During the permeability test, water molecules diffusing into the PGC samples via capillary are retained by the clinker aggregates. The trapped water molecules begin to hydrate with the clinker aggregates. As a result of these reactions, the porosity decreases as CSH structures are formed and fill the spaces in the internal structure. It was thought that the permeability values of the PGC samples with decreasing porosity decreased with the realization of the mentioned process.

Venkatesan and Pazhani (2016) investigated the strength and durability properties of geopolymer concrete prepared using blast furnace slag (GBFS) and black rice husk ash (BRHA) at different rates. According to the results of their experiments, adding more than 10% BRHA to the mixture reduces the strength values; permeability values decrease. Due to the chemical structure and dimensions of BRHA, filling the voids in the internal structure of the geopolymer concrete caused this situation to occur. Shaikh (2016) investigated the physical, mechanical and durability properties of fly ash based geopolymer concretes by using recycled coarse aggregate (RCA) at different rates. In his study, he observed that the permeability values of the mixtures increased with the increase of recycled coarse aggregate ratio. Due to the operations made during the production process of RCA, cracks occur on its surfaces. For this reason, it was interpreted that the permeability increased in geopolymer mixtures using RCA. Alcan et al. (2023) reported that in the geopolymer concrete they produced using GBFS and metakaolin, the permeability value decreased by 2.45 times as the curing time increased from 4 hours to 8 hours, and the permeability decreased by 81% when the curing temperature increased from 60 °C to 90 °C. Noushini and Castel (2016) investigated the permeability results of fly ash and slag-based geopolymer concretes after three different curing temperatures (60, 75 and 90 °C) and four different curing times (8, 12, 18 and 24 hours). As a result of their experiments, they stated that the mixtures cured at 75 °C for 18-24 hours had the lowest permeability value. They interpreted that lower porosity or less interconnected capillary spaces were formed because more gel products were formed at the mentioned curing temperature and time. Mermerdaş et al. (2017) added three types of aggregates, river sand, crushed limestone, and sand-limestone, to geopolymer concretes in which fly ash was used as binder. In their study, the best flowability was measured in groups with river sand aggregates, the best mechanical strength was measured in groups with limestone aggregates, and the lowest permeability results were measured in groups with sand-limestone aggregates. They observed the permeability value as 0.0222–0.0262 $mm/min^{0.5}$ in the groups where sand-limestone aggregate was used in combination. They interpreted this result as different types of aggregates filled the voids better with particles of various sizes and reduced their pore structures.

4. Conclusions

This study investigated the effects of clinker aggregate Prepacked geopolymer composite (PGC) applied at different curing temperatures and curing times on physical, mechanical and high temperature resistance. Obtained findings are presented below:

- While the curing time increased from 6 hours to 8 hours, the hardened unit weight values increased slightly; increasing the curing temperature from 30 °C to 60 °C increased these values at greater rates. Since clinker aggregate was added to GBFS weight removed from PGC mixture, the effect of clinker aggregate amount on unit weight values is not evident. The M1 mixture cured at 60 °C for 8 hours, with a hardened unit weight value of 2539.2 kg/m^3, the highest value observed.
- The compressive strength of PGC samples increased with increasing curing time and temperature. In particular, increasing the curing temperature from 30 °C to 60 °C made the increases in compressive strength more pronounced. Increasing clinker aggregate ratio, on the other hand, caused a decrease in strength. The highest compressive strength of 57.04 MPa belongs to the M3 mixture, which was cured at 60 °C for 8 hours; the lowest belongs to M8 mixture cured at 20.38 MPa 30 °C for 6 hours.
- The flexural strength results are quite similar to the compressive strength results. As more reaction products were formed with increasing curing temperature and time, the flexural strength increased. The M3 mixture, which is subjected to curing at 60 °C for 8 hours, is the highest value measured with a remarkable value of 9.93 MPa; The M8 mixture, cured at 30 °C for 6 hours with a value of 2.35 MPa, has the lowest flexural strength. The increase in the amount of clinker aggregate caused a decrease in the flexural strength.
- The strength of PGC samples after high temperature is directly proportional to curing temperature and curing time. The increase in clinker aggregates causes the formation of a hollower interior structure. In high temperature application, since the water vapor can move in the capillary spaces, the parasitic stresses are reduced. Thus, the strength loss rate is reduced. After 300 °C and 600 °C high temperature application, the highest strength is 25.17 MPa and 17.33 MPa, respectively, this belongs to the M3 mixture cured at 60 °C for 8 hours. The lowest strength values measured after the same high temperature are 15.21 MPa and

12.53 MPa, and the M8 group cured at 30 °C for 6 hours.

- Permeability values were highly affected by the change of clinker aggregate amount, curing temperature and curing time in the mixture. In case the applied curing temperature increased from 30 °C to 60 °C, the capillary water absorption values decreased significantly. Prolongation of the curing time also caused a similar effect. In PGC samples cured at higher temperature (60 °C) and longer (8 hours), since the porosity in the internal structure decreases; these results have been observed. The increase in the amount of clinker aggregate also decreased the permeability value. Clinker holds the water molecules in the aggregate permeability test and binds them to the calcium and silicate in its structure. As the resulting CSH structure fills the gaps, the internal structure of these groups becomes more compact. The M1 sample, which was cured for 6 hours at 30 °C, has the highest permeability value of 0.04 $kg/m^2.min^{0.5}$. In the M8 mixture cured at 60 °C for 8 hours, this value was measured as 0 $kg/m^2.min^{0.5}$.

This study tried to present a different perspective to the literature by combining Prepacked aggregate and geopolymer concrete technology with the use of clinker aggregate. It has been determined that this innovative type of concrete can be used in works such as underwater concrete casting and repair, and can increase high temperature resistance. The study aims to make the mentioned technology more sustainable by making some suggestions for the authors who will conduct research on this subject in the future.

Acknowledgements

None declared.

Funding

The authors received no financial support for the research, authorship, and/or publication of this manuscript.

Conflict of Interest

The authors declared no potential conflicts of interest with respect to the research, authorship, and/or publication of this manuscript.

References

Ahmed HU, Mohammed AS, Qaidi SM, Faraj RH, Hamah Sor N, Mohammed A (2022). Compressive strength of geopolymer concrete composites: a systematic comprehensive review, analysis and modeling. *European Journal of Environmental and Civil Engineering*, 1-46.

Aïtcin PC (2000). Cements of yesterday and today: concrete of tomorrow. *Cement and Concrete Research*, 30(9), 1349-1359.

Albitar M., Ali MM, Visintin P, Drechsler M (2017). Durability evaluation of geopolymer and conventional concretes. *Construction and Building Materials*, 136, 374-385.

Alcan HG, Bayrak B, Öz A, Kavaz E, Kaplan G, Çelebi O, Aydın AC (2023). A comprehensive characterization on geopolymer concretes with low content slag and quartz aggregates: the shielding features. *Radiation Effects and Defects in Solids*, 1-30.

Aldanmaz BA (2020). Karma Lifli betonların tek eksenli çekme altında çatlak yapısının incelenmesi. *Teknik Dergi,* 31(1), 9773-9787.

Amran M, Debbarma S, Ozbakkaloglu T (2021). Fly ash-based eco-friendly geopolymer concrete: A critical review of the long-term durability properties. *Construction and Building Materials*, 270, 121857.

Aredes F, Campos T, Machado J, Sakane K, Thim G, Brunelli D (2015). Effect of cure temperature on the formation of metakaolinite-based geopolymer. *Ceramics International,* 41(6), 7302-7311.

Arioz O (2009). Retained properties of concrete exposed to high temperatures: Size effect. *Fire and Materials: An International Journal,* 33(5), 211-222.

ASTM C348 (2008). Standard test method for flexural strength of hydraulic-cement mortars. ASTM C348-02, Annu book ASTM Stand 04.01.

ASTM C349 (2008). Standard test method for compressive strength of hydraulic cement mortar (using portions of prisms broken in flexure), West Conshohocken (PA): ASTM International.

ASTM C642 (2006). Standard test method for density, absorption, and voids in hardened concrete. American Society for Testing of Materials, Annual Book of ASTM Standards, vol. 04.02, Philadelphia.

ASTM C989 (2006). Standard specification for ground granulated blast furnace slag for use in concrete and mortars. vol. 4.02.

Aydin AC, Arslan A, Gül R (2007). Mesoscale simulation of cement based materials' time-dependent behavior. *Computational Materials Science*, 41(1), 20-26.

Barcelo L, Kline J, Walenta G, Gartner E (2014). Cement and carbon emissions. *Materials and Structures,* 47(6), 1055-1065.

Behnood A. Ghandehari M, (2009). Comparison of compressive and splitting tensile strength of high-strength concrete with and without polypropylene fibers heated to high temperatures. *Fire Safety Journal,* 44(8), 1015-1022.

Benhelal E, Zahedi G, Shamsaei E, Bahadori A (2013). Global strategies and potentials to curb CO_2 emissions in cement industry. *Journal of Cleaner Production,* 51, 142-161.

Berger R (1974). Properties of concrete with cement clinker aggregate. *Cement and Concrete Research,* 4(1), 99-112.

Beshr H, Almusallam A, Maslehuddin M, (2003). Effect of coarse aggregate quality on the mechanical properties of high strength concrete. *Construction and Building Materials,* 17(2), 97-103.

Chan Y, Peng G, Anson M (1999). Residual strength and pore structure of high-strength concrete and normal strength concrete after exposure to high temperatures. *Cement and Concrete Composites,* 21(1), 23-27.

Cheng Y, Liu S, Zhu B, Liu R, Wang Y (2019). Preparation of preplaced aggregate concrete and experimental study on its strength. *Construction and Building Materials,* 229, 116847.

Das KK, Lam ES, Tang HH (2021). Partial replacement of cement by ground granulated blast furnace slag and silica fume in two-stage concrete (preplaced aggregate concrete). *Structural Concrete*, 22, E466-E473.

De Castro S, de Brito J (2013). Evaluation of the durability of concrete made with crushed glass aggregates. *Journal of Cleaner Production*, 41, 7-14.

Domingo-Cabo A, Lázaro C, López-Gayarre F, Serrano-López M, Serna P, Castaño-Tabares JO (2009). Creep and shrinkage of recycled aggregate concrete. *Construction and Building Materials*, 23(7), 2545-2553.

Durak U (2022). Effect of short-term elevated temperature curing on strength properties and microstructure of fresh fly ash geopolymer mortar. *Arabian Journal of Geosciences,* 15(9), 810.

EN 1015-18 (2002). Methods of Test for Mortar for Masonry—Part 18: Determination of Water Absorption Coefficient Due to Capillary Action of Hardened Mortar.

Golewski GL (2021). Green concrete based on quaternary binders with significant reduced of CO_2 emissions. *Energies,* 14(15), 4558.

Gültekin A, Hosseinnezhad H, Ramyar K (2022). Agrega türünün geopolimer betonun yüksek sıcaklık direncine etkisi. *Politeknik Dergisi*, 1-1.

Güzelküçük S, Demir İ (2019). Perlit Esaslı Geopolimer Kompozitlere Kür Süresi Ve Sıcaklığın Etkisi. *International Journal of Engineering Research and Development*, 11(2), 730-737.

Hager I, Sitarz M, Mróz K (2021). Fly-ash based geopolymer mortar for high-temperature application–Effect of slag addition. *Journal of Cleaner Production*, 316, 128168.

Hassan A, Arif M, Shariq M (2019). Effect of curing condition on the mechanical properties of fly ash-based geopolymer concrete. *SN Applied Sciences*, 1, 1-9.

Huo J, Zheng Q, Chen B, Xiao Y (2009). Tests on impact behaviour of micro-concrete-filled steel tubes at elevated temperatures up to 400 C. *Materials and Structures*, 42, 1325-1334.

Jindal BB, Alomayri T, Hasan A, Kaze CR (2022). Geopolymer concrete with metakaolin for sustainability: a comprehensive review on raw material's properties, synthesis, performance, and potential application. *Environmental Science and Pollution Research*, 1-26.

Kaplan G, Shi J, Öz A, Bayrak B, M. Dheyaaldin MH, Aydın AC (2023). Preparation and characterization of a novel prepacked aggregate geopolymer: A feasibility study. *Powder Technology*, 421, 118423.

Khalid HR, Lee N, Choudhry I, Wang Z, Lee HK (2019). Evolution of zeolite crystals in geopolymer-supported zeolites: Effects of composition of starting materials. *Materials Letters,* 239, 33-36.

Khayat KH (1999). Workability, testing, and performance of self-consolidating concrete. *Materials Journal,* 96(3), 346-353.

Krishna R, Mishra J, Zribi M, Adeniyi F, Saha S, Baklouti S, Shaikh FUA Gökçe H (2021). A review on developments of environmentally friendly geopolymer technology. *Materialia,* 20, 101212.

Kürklü G (2016). The effect of high temperature on the design of blast furnace slag and coarse fly ash-based geopolymer mortar. *Composites Part B: Engineering,* 92, 9-18.

Lv J, Zhou T, Li K (2020). Development and investigation of a new low-cement-consumption concrete—Preplaced aggregate concrete. *Sustainability,* 12(3), 1080.

Mermerdaş K, Manguri S, Nassani DE, Oleiwi SM (2017). Effect of aggregate properties on the mechanical and absorption characteristics of geopolymer mortar. *Engineering Science and Technology, An International Journal,* 20(6), 1642-1652.

Meyer CJC (2009). The greening of the concrete industry. *Cement and Concrete Composites,* 31(8), 601-605.

Mo B, Zhu H, Cui X, He Y, Gong S (2014). Effect of curing temperature on geopolymerization of metakaolin-based geopolymers. *Applied Clay Science,* 99, 144-148.

Mohammed AA, Ahmed HU, Mosavi A (2021). Survey of mechanical properties of geopolymer concrete: a comprehensive review and data analysis. *Materials,* 14(16), 4690.

Noumowe A, (2005). Mechanical properties and microstructure of high strength concrete containing polypropylene fibres exposed to temperatures up to 200 C. *Cement and Concrete Research,* 35(11), 2192-2198.

Noushini A, Castel A (2016). The effect of heat-curing on transport properties of low-calcium fly ash-based geopolymer concrete. *Construction and Building Materials*, 112, 464-477.

Nuaklong P, Worawatnalunart P, Jongvivatsakul P, Tangaramvong S, Pothisiri T, Likitlersuang S (2021). Pre-and post-fire mechanical performances of high calcium fly ash geopolymer concrete containing granite waste. *Journal of Building Engineering*, 44, 103265.

Öz A, Bayrak B, Kavaz E, Kaplan G, Çelebi O, Alcan HG, Aydın AC (2022). The radiation shielding and microstructure properties of quartzic and metakaolin based geopolymer concrete. *Construction and Building Materials*, 342, 127923.

Prokopski G, Halbiniak J (2000). Interfacial transition zone in cementitious materials. *Cement and Concrete Research*, 30(4), 579-583.

Raza A, Ouni MHE, Azab M, Ali K, Haider H, Rashedi A (2022). A scientometric review on mechanical and durability performance of geopolymer Paste: Effect of various raw materials. *Construction and Building Materials*, 345, 128297.

Samal S, (2019). Effect of high temperature on the microstructural evolution of fiber reinforced geopolymer composite. *Heliyon*, 5(5), e01779.

Schneider U, (1988). Concrete at high temperatures—a general review. *Fire Safety Journal,* 13(1), 55-68.

Sevinç AH, Durgun MY (2020). Properties of high-calcium fly ash-based geopolymer concretes improved with high-silica sources. *Construction and Building Materials*, 261, 120014.

Shafaghat J, Allahverdi A (2019). Enhancing concrete properties by using silica fume as reactive powder and portland cement-clinker as reactive aggregate. *Journal of Materials in Civil Engineering*, 31(11), 04019278.

Shaikh FUA (2016). Mechanical and durability properties of fly ash geopolymer concrete containing recycled coarse aggregates. *International Journal of Sustainable Built Environment*, 5(2), 277-287.

Suhendro B (2014). Toward green concrete for better sustainable environment. *Procedia Engineering*, 95: 305-320.

Sukontasukkul P, Pomchiengpin W, Songpiriyakij S (2010). Post-crack (or post-peak) flexural response and toughness of fiber reinforced concrete after exposure to high temperature. *Construction and Building Materials,* 24(10), 1967-1974.

Tayeh BA, Zeyad AM, IAgwa IS, Amin M (2021). Effect of elevated temperatures on mechanical properties of lightweight geopolymer concrete. *Case Studies in Construction Materials*, 15: e00673.

Titi HH, Tabatabai H (2018). Effect of coarse aggregate type on chloride ion penetration in concrete. *Construction and Building Materials,* 162, 871-880.

Topçu İB, Canbaz M (2008). Silis dumanının betonda mekanik çatlak oluşumlarına etkisi. *Eskişehir Osmangazi Üniversitesi Mühendislik ve Mimarlık Fakültesi Dergisi*, 21(2), 17-26.

Van Deventer JS, Provis JL, Duxson P, Brice DG (2010). Chemical research and climate change as drivers in the commercial adoption of alkali activated materials. *Waste and Biomass Valorization*, 1, 145-155.

Van Jaarsveld J, Van Deventer JS, Lukey G (2002). The effect of composition and temperature on the properties of fly ash-and kaolinite-based geopolymers. *Chemical Engineering Journal,* 89(1-3), 63-73.

Venkatesan RP, Pazhani K (2016). Strength and durability properties of geopolymer concrete made with ground granulated blast furnace slag and black rice husk ash. *KSCE Journal of Civil Engineering,* 20, 2384-2391.

Verma M, Dev N (2022). Effect of ground granulated blast furnace slag and fly ash ratio and the curing conditions on the mechanical properties of geopolymer concrete. *Structural Concrete*, 23(4), 2015-2029.

Wakeley L, Roy D (1983). Experimental concretes for sealing radioactive-waste repositories in evaporite strata. *Cement and Concrete Research*, 13(1), 97-106.

Wasim M, Ngo TD, Law D (2021). A state-of-the-art review on the durability of geopolymer concrete for sustainable structures and infrastructure. *Construction and Building Materials,* 291, 123381.

Winnefeld F, Leemann A, German A, Lothenbach B (2022). CO_2 storage in cement and concrete by mineral carbonation. *Current Opinion in Green and Sustainable Chemistry*, 100672.

Worrell E, Price L, Martin N, Hendriks C, Meida LO (2001). Carbon dioxide emissions from the global cement industry. *Annual Review of Energy and the Environment,* 26(1), 303-329.

Yoon J, Kim H, Shin SW, Sim SH (2020). Rheology-based determination of injectable grout fluidity for preplaced aggregate concrete using ultrasonic tomography. *Construction and Building Materials*, 260, 120447.

Zhang C, Wang X, Hu Z, Wu Q, Zhu H, Lu J (2021). Long-term performance of silane coupling agent/metakaolin based geopolymer. *Journal of Building Engineering*, 36, 102091.

Zhang G, Yang H, Ju C, Yang Y (2020). Novel selection of environment-friendly cementitious materials for winter construction: Alkali-activated slag/Portland cement. *Journal of Cleaner Production,* 258, 120592.

Challenge Journal of Structural Mechanics

Research Article

Three-dimensional static analysis of reinforced concrete cantilever beam using MATLAB Partial Differential Equation Toolbox

Olgun Köksal [a], Zeki Karaca [b], Erdem Türkeli [c,*]

[a] *Kavak Vocational School, Construction Department, Samsun University, 55850 Samsun, Türkiye*
[b] *Department of Civil Engineering, Ondokuz Mayıs University, 55270 Samsun, Türkiye*
[c] *Vocational School of Technical Sciences, Construction Department, Ordu University, 52200 Ordu, Türkiye*

ABSTRACT

Nowadays, three-dimensional (3D) solid model of the structures can be prepared by using computer aided design programs. There are many numerical methods for static, dynamic and temperature analysis of structural systems. The most preferred among these methods is the finite element method (FEM). In this method, the structural model with different geometry and boundary conditions should be solved by utilizing partial differential equations. Due to the long solution time while performing, finite element programs require computers with very good features. Therefore, analyses with desired features can be performed by using open source programs to shorten the duration of analysis. In this study, specifically, the static analysis of the selected reinforced concrete (RC) cantilever beam was carried out by using the open source MATLAB partial differential toolbox based on the FEM. Since the program used is open source, different concrete classes and finite element models were selected for the cited cantilever beam and static analyses were performed. As a result of the MATLAB partial differential toolbox analyses, the displacement, stress and deformation of the cantilever beam were obtained in 3D and compared with the ones obtained from ANSYS computer program.

ARTICLE INFO

Article history:
Received 6 May 2023
Revised 13 July 2023
Accepted 8 August 2023

Keywords:
Finite element method
Static analysis
Partial Differential Equation Toolbox
Cantilever beam

1. Introduction

With the development of computer technology in the last fifty years, modeling of structural systems and examining their behavior under external loads have attracted the attention of many researchers. Previously, the ideal conditions of the structural systems were determined and solutions were obtained with traditional analysis methods. Many new numerical methods have been the subject of theoretical research due to the fact that traditional methods solve plane problems, the results are approximate, the solution times are longer, they can work in certain geometries, and the choice of materials is limited (Argyris and Kelsey 1960). Among these methods, the FEM is one of the most preferred method today. FEM is a numerical method used to solve engineering and mathematical physics problems. By using this numerical method, problems in many fields such as structural mechanics and dynamics, fluid mechanics and dynamics, heat transfer, diffusion and electrostatics are solved. In the FEM method, it is desired to divide the engineering problem into small parts. Matrix solutions are realized by reflecting the contribution of these small parts from external effects and boundary conditions to the whole system. As a result of the solutions, displacement, stress and strain are obtained at a finite number of nodes (Kasımzade 2018).

FEM was first used in 1956 to solve space problems (Turner et al. 2012). With the development of computer technology, FEM started to take itself to the forefront in the 1970s (Bathe and Wilson 1976; Gallagher 1975; Oden and Sato 1967; Zienkiewicz 1972). Many researchers have prepared computer programs based on this method. Today, there are many finite element software

* *Corresponding author*. Tel.: +90-452-233-4865 ; Fax: +90-452-233-5230 ; E-mail address: erdemturkeli@odu.edu.tr (E. Türkeli)
ISSN: 2149-8024 / DOI: https://doi.org/10.20528/cjsmec.2023.03.003

prepared by both commercial companies and academicians (Kasımzade 2018). Since the program codes of commercial software for academic studies are generally not open source, academicians prefer open source software. In this study, linear static analysis of a RC cantilever beam was performed using MATLAB Partial Differential Equation Toolbox based on the FEM (MATLAB R2023a 2023). By selecting different strength classes for concrete and different types of finite elements, displacement, stress and strain results are presented.

2. Material and Method

2.1. MATLAB Partial Differential Equation Toolbox

The Partial Differential Equation Toolbox (PDE Toolbox) (Fig. 1) provides functions for solving structural mechanics, heat transfer, and general partial differential equations (PDEs) using the finite element method (MATLAB R2023a 2023) .

Features of this cited toolbox (MATLAB R2023a 2023);

- It can be used to calculate deformations and stresses.
- For modeling the dynamics and vibration of the structure, the toolbox has a time-integrating solver directly.
- It can analyze the structural properties of a component by performing modal analysis to find natural frequencies and mode shapes.
- It can model conductive heat transfer problems to calculate heat distributions, heat flow and heat flow rates over surfaces.
- It can also solve standard problems such as diffusion, electrostatics, magnetostatics and special PDEs.
- Imports 2D and 3D geometries using mesh data.
- It can automatically create meshes with triangular and tetrahedral elements.

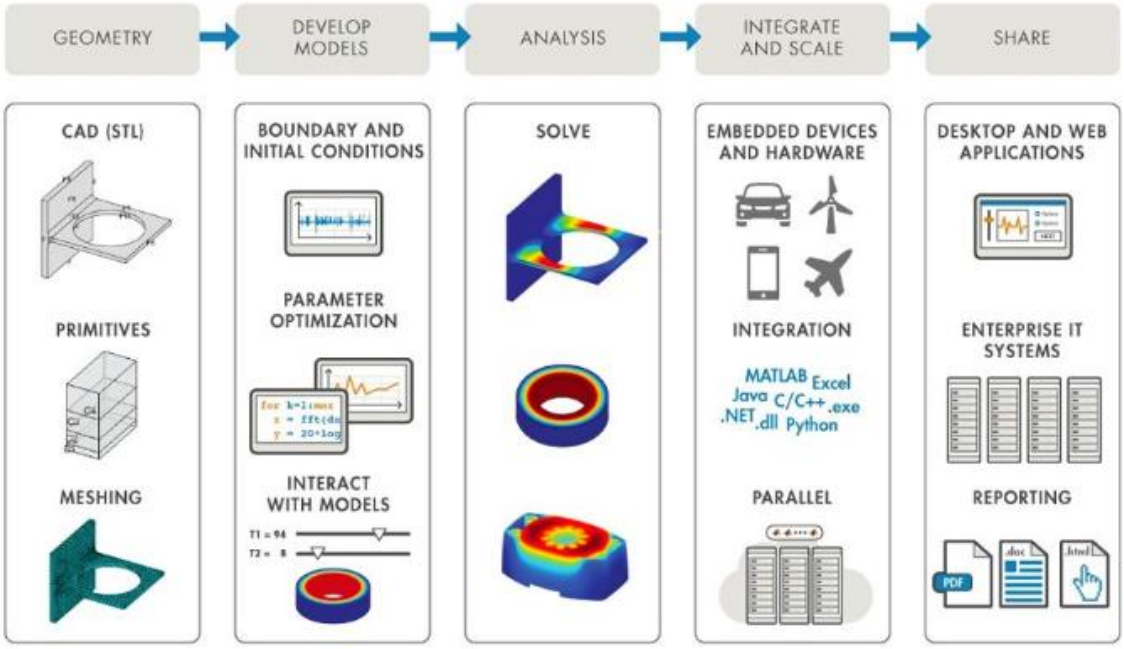

Fig. 1. The flowchart of PDE Toolbox (MATLAB R2023a 2023).

The PDE toolbox calculates equations in the form given below (MATLAB R2023a 2023).

$$m\frac{\partial^2 u}{\partial t^2} + d\frac{\partial u}{\partial t} \cdot \nabla \cdot (c\nabla u) + au = f \quad (1)$$

$$\nabla \cdot (c\nabla u) + au = \lambda du \quad (2)$$

$$\nabla \cdot (c\nabla u) + au = \lambda^2 mu \quad (3)$$

Eq. (3) solves eigenvalue problems. When solving PDEs, there are two boundary choices for each edge or face. Dirichlet boundary conditions performs the solution equation at the edge or surface.

$$hu = r \quad (4)$$

where, h and r are denoting 3D (x, y, z) space functions. Generalized Neumann boundary conditions performs the solution equation at the edge or surface.

$$\vec{n} \cdot (c\nabla u) + qu = g \quad (5)$$

$\vec{n}$ is denoting the unit normal vector. q and g are functions defined in $\partial\Omega$ depending on (x, y, z) in 3D space.

2.2. Linear equations of elasticity

In linear elasticity, the stiffness matrix of an isotropic material depends on two parameters, E, representing Young's modulus and ν, Poisson's ratio. Equilibrium equation in static condition is given in Eq. (6).

$$-\nabla.\sigma = f \quad (6)$$

The relationship between linearized small displacements and strains is given with Eq. (7).

$$\varepsilon = \frac{1}{2}(\nabla u + \nabla u^T) \tag{7}$$

The angular momentum equilibrium shows that the stress is symmetrical.

$$\sigma_{ij} = \sigma_{ji} \tag{8}$$

According to the linear elasticity theory, the relationship between stress and strain is as follows.

$$\begin{bmatrix}\sigma_{11}\\ \sigma_{22}\\ \sigma_{33}\\ \sigma_{23}\\ \sigma_{13}\\ \sigma_{12}\end{bmatrix} = \frac{E}{(1-\nu)(1-2\nu)}\begin{bmatrix}1-\nu & \nu & \nu & 0 & 0 & 0\\ \nu & 1-\nu & \nu & 0 & 0 & 0\\ \nu & \nu & 1-\nu & 0 & 0 & 0\\ 0 & 0 & 0 & 1-2\nu & 0 & 0\\ 0 & 0 & 0 & 0 & 1-2\nu & 0\\ 0 & 0 & 0 & 0 & 0 & 1-2\nu\end{bmatrix}\begin{bmatrix}\varepsilon_{11}\\ \varepsilon_{22}\\ \varepsilon_{33}\\ \varepsilon_{23}\\ \varepsilon_{13}\\ \varepsilon_{12}\end{bmatrix} \tag{9}$$

If written in expanded form, Eq. (10) is obtained in which • shows the symmetricity.

$$\begin{bmatrix}\sigma_{11}\\ \sigma_{12}\\ \sigma_{13}\\ \sigma_{21}\\ \sigma_{22}\\ \sigma_{23}\\ \sigma_{31}\\ \sigma_{32}\\ \sigma_{33}\end{bmatrix} = \frac{E}{(1-\nu)(1-2\nu)}\begin{bmatrix}1-\nu & 0 & 0 & 0 & \nu & 0 & 0 & 0 & \nu\\ \bullet & 1-2\nu & 0 & 0 & 0 & 0 & 0 & 0 & 0\\ \bullet & \bullet & 1-2\nu & 0 & 0 & 0 & 0 & 0 & 0\\ \bullet & \bullet & \bullet & 1-2\nu & 0 & 0 & 0 & 0 & 0\\ \bullet & \bullet & \bullet & \bullet & 1-\nu & 0 & 0 & 0 & \nu\\ \bullet & \bullet & \bullet & \bullet & \bullet & 1-2\nu & 0 & 0 & 0\\ \bullet & \bullet & \bullet & \bullet & \bullet & \bullet & 1-2\nu & 0 & 0\\ \bullet & \bullet & \bullet & \bullet & \bullet & \bullet & \bullet & 1-2\nu & 0\\ \bullet & \bullet & \bullet & \bullet & \bullet & \bullet & \bullet & \bullet & 1-\nu\end{bmatrix} \tag{10}$$

2.3. Three-dimensional linear equations of elasticity

If Eq. (6) is written for MATLAB PDE Toolbox, Eq. (11) is obtained.

$$-\nabla(c \otimes \nabla u) = f \tag{11}$$

$$\varepsilon = \frac{1}{2}(\nabla u + \nabla u^T) \tag{12}$$

Strain depends on both ∇u and its transpose. If it is necessary to convert this from strain to ∇u, and the column is written in vector form, Eq. (13) can be obtained.

$$\nabla u = \begin{bmatrix}\partial u_x/\partial x\\ \partial u_x/\partial y\\ \partial u_x/\partial z\\ \partial u_y/\partial x\\ \partial u_y/\partial y\\ \partial u_y/\partial z\\ \partial u_z/\partial x\\ \partial u_z/\partial y\\ \partial u_z/\partial z\end{bmatrix} \tag{13}$$

After that, the deformation-displacement relationship can be written in Eqs. (14)-(20):

$$\varepsilon = \begin{bmatrix}1 & 0 & 0 & 0 & 0 & 0 & 0 & 0 & 0\\ 0 & 1/2 & 0 & 1/2 & 0 & 0 & 0 & 0 & 0\\ 0 & 0 & 1/2 & 0 & 0 & 0 & 1/2 & 0 & 0\\ 0 & 1/2 & 0 & 1/2 & 0 & 0 & 0 & 0 & 0\\ 0 & 0 & 0 & 0 & 1 & 0 & 0 & 0 & 0\\ 0 & 0 & 0 & 0 & 0 & 1/2 & 0 & 0 & 0\\ 0 & 0 & 1/2 & 0 & 0 & 0 & 1/2 & 0 & 0\\ 0 & 0 & 0 & 0 & 0 & 1/2 & 0 & 1/2 & 0\\ 0 & 0 & 0 & 0 & 0 & 0 & 0 & 0 & 1\end{bmatrix} \nabla u \equiv A\nabla u \tag{14}$$

$$\sigma = \frac{E}{(1-\nu)(1-2\nu)} \begin{bmatrix} 1-\nu & 0 & 0 & 0 & \nu & 0 & 0 & 0 & \nu \\ \bullet & 1-2\nu & 0 & 0 & 0 & 0 & 0 & 0 & 0 \\ \bullet & \bullet & 1-2\nu & 0 & 0 & 0 & 0 & 0 & 0 \\ \bullet & \bullet & \bullet & 1-2\nu & 0 & 0 & 0 & 0 & 0 \\ \bullet & \bullet & \bullet & \bullet & 1-\nu & 0 & 0 & 0 & \nu \\ \bullet & \bullet & \bullet & \bullet & \bullet & 1-2\nu & 0 & 0 & 0 \\ \bullet & \bullet & \bullet & \bullet & \bullet & \bullet & 1-2\nu & 0 & 0 \\ \bullet & \bullet & \bullet & \bullet & \bullet & \bullet & \bullet & 1-2\nu & 0 \\ \bullet & \bullet & \bullet & \bullet & \bullet & \bullet & \bullet & \bullet & 1-\nu \end{bmatrix} A\nabla u \tag{15}$$

$$\sigma = \frac{E}{(1-\nu)(1-2\nu)} \begin{bmatrix} 1-\nu & 0 & 0 & 0 & \nu & 0 & 0 & 0 & \nu \\ 0 & 1/2-\nu & 0 & 1/2-\nu & 0 & 0 & 0 & 0 & 0 \\ 0 & 0 & 1/2-\nu & 0 & 0 & 0 & 1/2-\nu & 0 & 0 \\ 0 & 1/2-\nu & 0 & 1/2-\nu & 0 & 0 & 0 & 0 & 0 \\ \nu & 0 & 0 & 0 & 1-\nu & 0 & 0 & 0 & \nu \\ 0 & 0 & 0 & 0 & 0 & 1-2\nu & 0 & 1-2\nu & 0 \\ 0 & 0 & 1/2-\nu & 0 & 0 & 0 & 1-2\nu & 0 & 0 \\ 0 & 0 & 0 & 0 & 0 & 1/2-\nu & 0 & 1-2\nu & 0 \\ \nu & 0 & 0 & 0 & \nu & 0 & 0 & 0 & 1-\nu \end{bmatrix} \nabla u \tag{16}$$

$$\mu = \frac{E}{2(1+\nu)} \tag{17}$$

$$\lambda = \frac{E\nu}{(1+\nu)(1-2\nu)} \tag{18}$$

$$2\mu + \lambda = \frac{E(1-\nu)}{(1+\nu)(1-2\nu)} \tag{19}$$

Equalities are obtained. If rearranged accordingly, Eq. (20) can be obtained.

$$\sigma = \begin{bmatrix} 2\mu+\lambda & 0 & 0 & 0 & \lambda & 0 & 0 & 0 & \lambda \\ 0 & \mu & 0 & \mu & 0 & 0 & 0 & 0 & 0 \\ 0 & 0 & \mu & 0 & 0 & 0 & \mu & 0 & 0 \\ 0 & \mu & 0 & \mu & 0 & 0 & 0 & 0 & 0 \\ \lambda & 0 & 0 & 0 & 2\mu+\lambda & 0 & 0 & 0 & \lambda \\ 0 & 0 & 0 & 0 & 0 & \mu & 0 & \mu & 0 \\ 0 & 0 & \mu & 0 & 0 & 0 & \mu & 0 & 0 \\ 0 & 0 & 0 & 0 & 0 & \mu & 0 & \mu & 0 \\ \lambda & 0 & 0 & 0 & \lambda & 0 & 0 & 0 & 2\mu+\lambda \end{bmatrix} \nabla u \equiv c\nabla u \tag{20}$$

The equation for the von Mises yield criterion is given below (McDowell and Ellis 1993; Jones 2009).

$$\sigma_v = \sqrt{\frac{1}{2}\left[\left(\sigma_{xx}-\sigma_{yy}\right)^2 + \left(\sigma_{yy}-\sigma_{zz}\right)^2 + (\sigma_{zz}-\sigma_{xx})^2 + 6\left(\sigma_{xy}^2+\sigma_{yz}^2+\sigma_{zx}^2\right)^2\right]} \tag{21}$$

$$\varepsilon_v = \frac{1}{\sqrt{2}(1+\upsilon)}\sqrt{\left[\left(\varepsilon_{xx}-\varepsilon_{yy}\right)^2 + \left(\varepsilon_{yy}-\varepsilon_{zz}\right)^2 + (\varepsilon_{zz}-\varepsilon_{xx})^2 + \frac{3}{2}\left(\gamma_{xy}^2+\gamma_{yz}^2+\gamma_{zx}^2\right)^2\right]} \tag{22}$$

2.4. RC cantilever beam

Cantilever beams are often needed in civil engineering applications. As an example, a RC cantilever beam was chosen as in Fig. 2 (Doğangün 2020). The RC cantilever beam in Fig. 2 has a rectangular section with a span of L=2.00m, a width of b=0.25m, and a height of h=0.50m. The cantilever beam is loaded with a distributed load of q=100kN/m. Point A is fixed support, point B has no support.

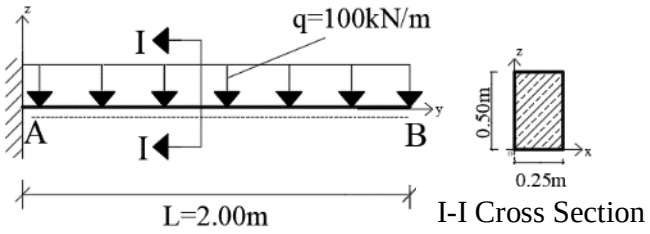

Fig. 2. Geometric properties and loading conditions of RC cantilever beam.

The material properties to be used for the static analysis of the cited RC cantilever beam are also given in Table 1.

In Fig. 3(a), the 3D solid model of the cantilever beam was created with the MATLAB PDE toolbox. The material properties of the RC cantilever beam are coded according to Table 1. Fig. 3(b) shows 3D linear tetrahedral solid finite element modeling for cantilever beam constructed in ANSYS (2016). The finite element model of the cantilever beam provided in Fig. 3(b) has a total of 966 nodes and 3852 finite elements.

Table 1. Material properties of RC cantilever beam (UNE EN 1992-1-2:2011/A1:2021 Eurocode 2: n.d.).

Concrete class	Characteristic cylinder compressive strength (MPa)	Characteristic cube compressive strength (MPa)	Elasticity module (MPa)	Poisson ratio	Unit volume weight (kN/m³)
C25/30	25	30	31476	0.2	25
C30/37	30	37	32837	0.2	25
C35/45	35	45	34077	0.2	25
C40/50	40	50	35220	0.2	25
C45/55	45	55	36283	0.2	25

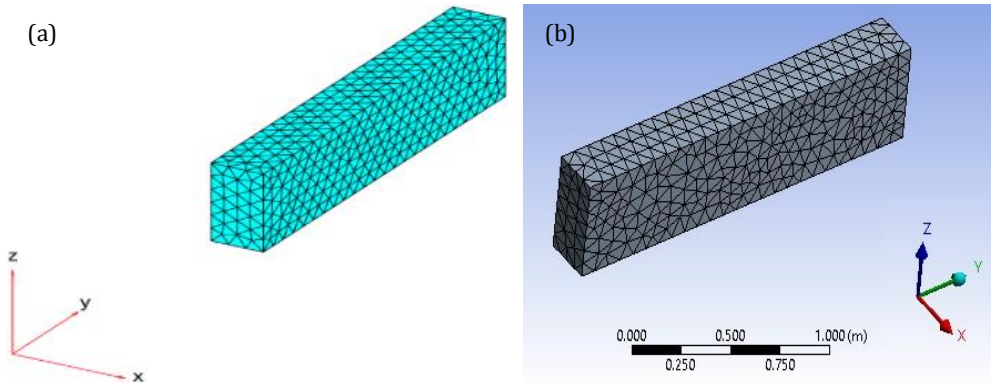

Fig. 3. RC cantilever beam: (a) 3D solid model (MATLAB); (b) mesh with linear tetrahedral solid elements (ANSYS).

3. Findings and Discussion

In this section of the study, displacement, deformation and stress distributions obtained for different concrete classes (using MATLAB PDE Toolbox) of the cited RC cantilever beam are provided in Figs. 4-13.

In addition, for different concrete classes, the separate analysis results given in Figs. 4-13 are provided collectively in Figs. 14-21.

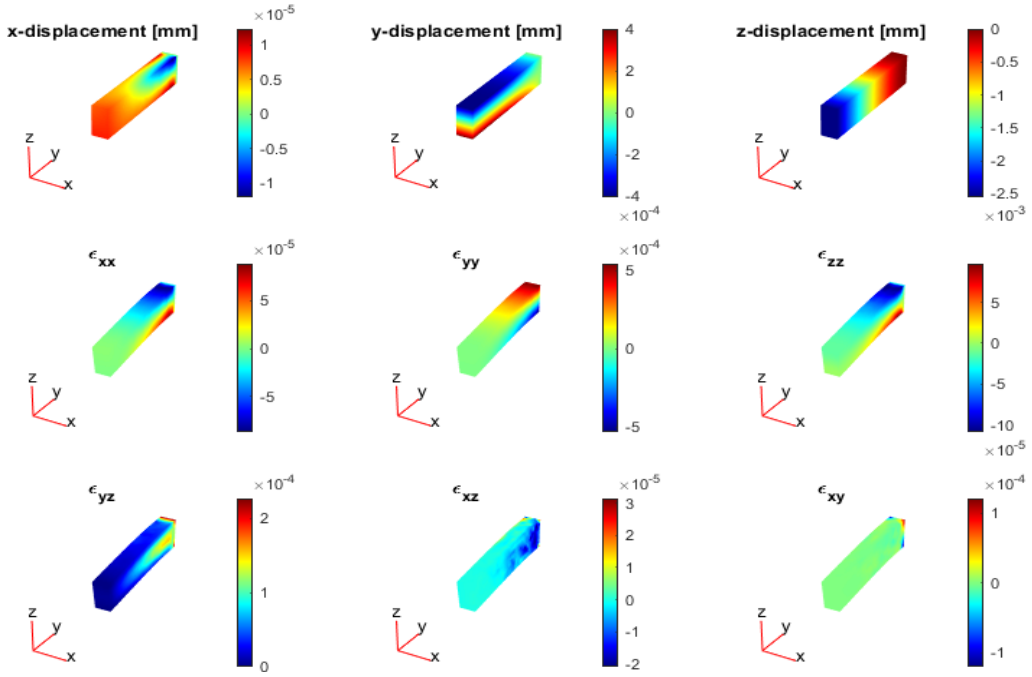

Fig. 4. Displacement and deformation results of C25/30 RC cantilever beam.

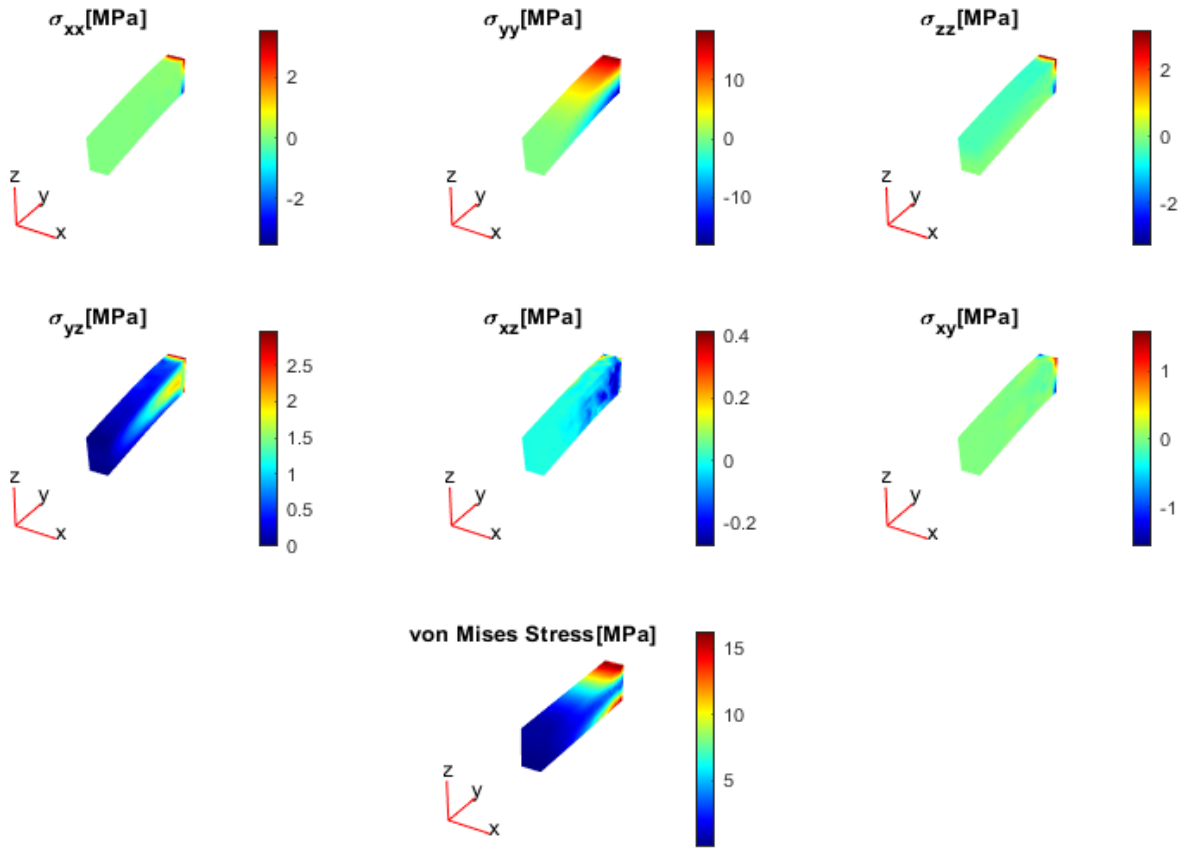

Fig. 5. Stress results of C25/30 RC cantilever beam.

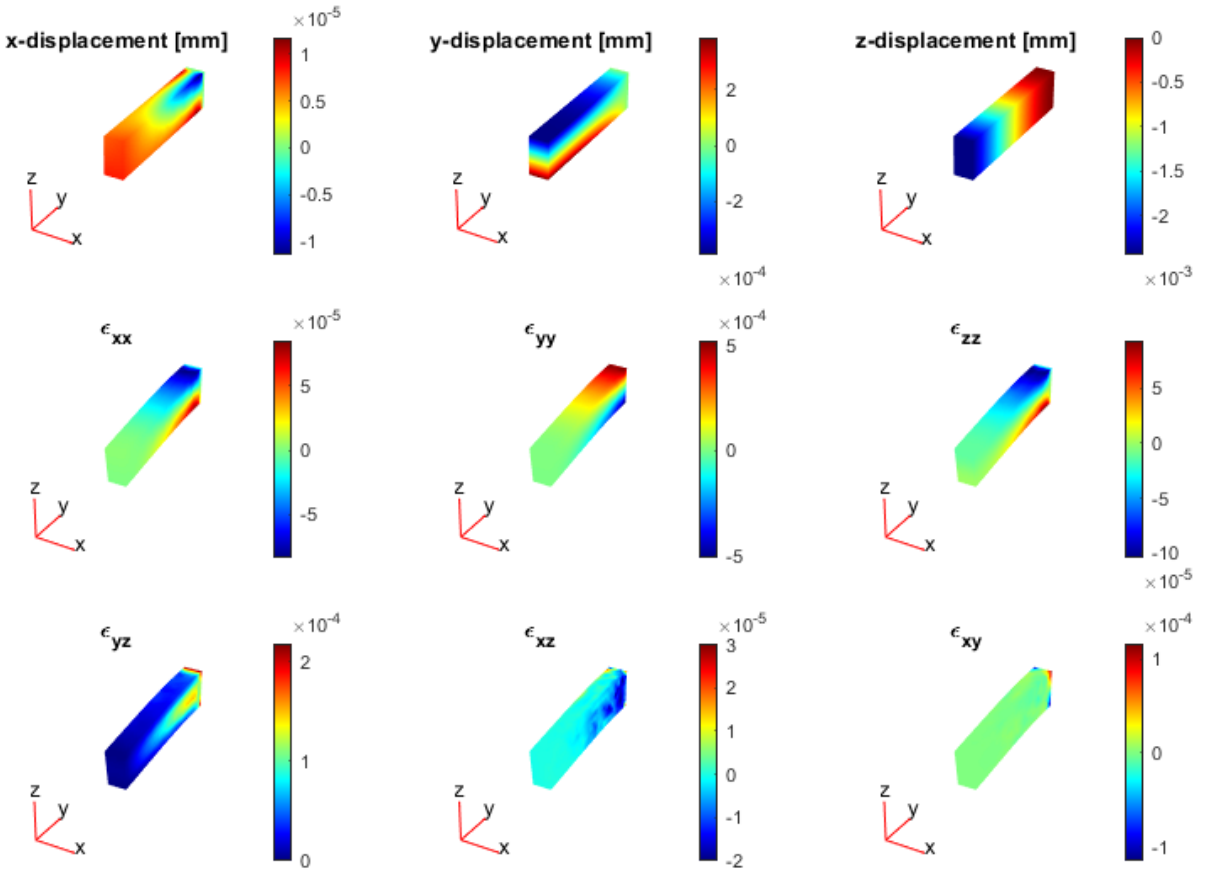

Fig. 6. Displacement and deformation results of C30/37 RC cantilever beam.

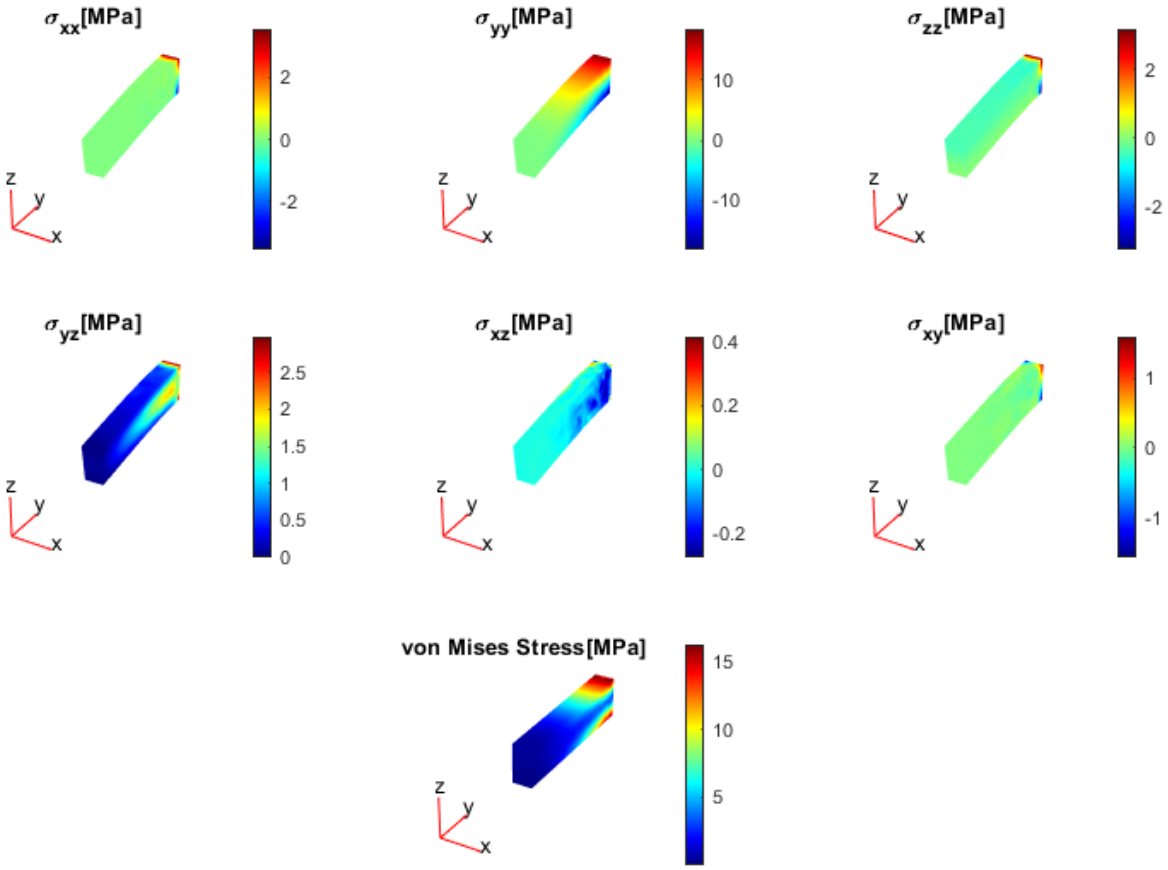

Fig. 7. Stress results of C30/37 RC cantilever beam.

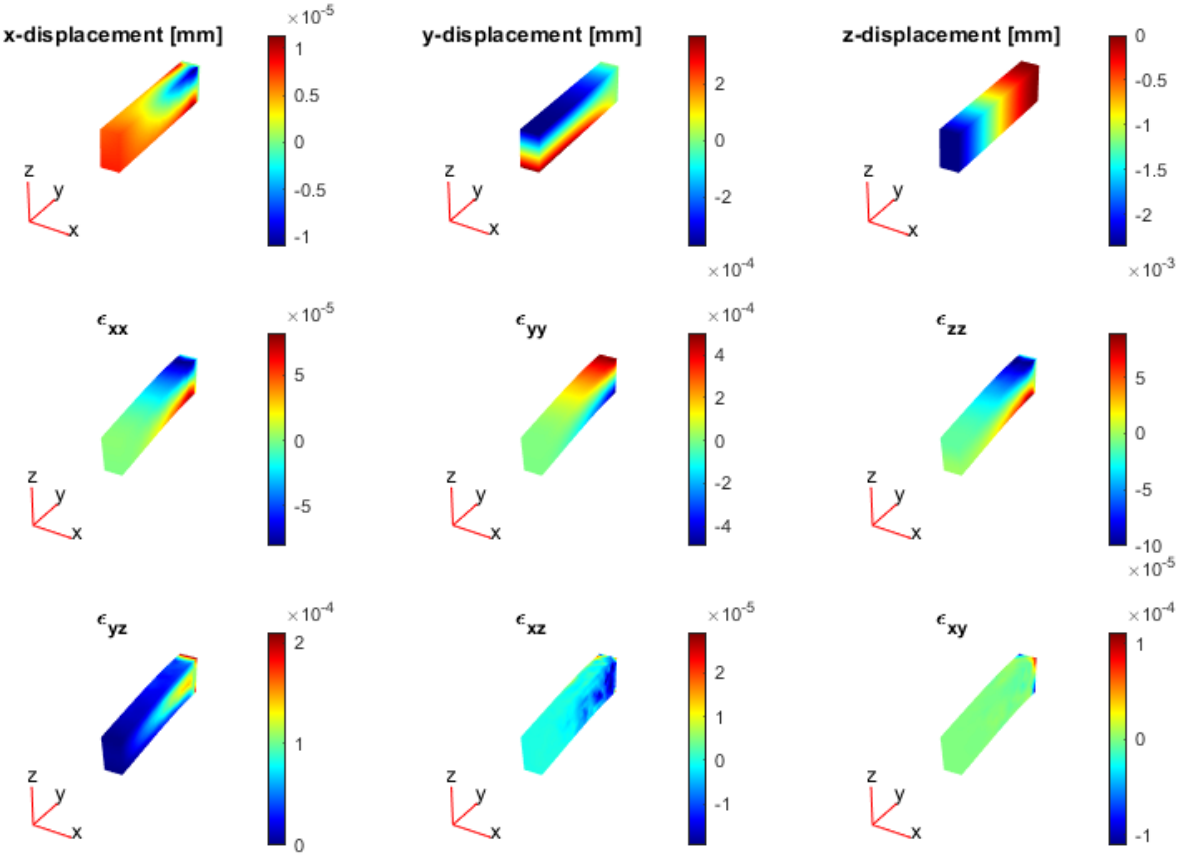

Fig. 8. Displacement and deformation results of C35/45 RC cantilever beam.

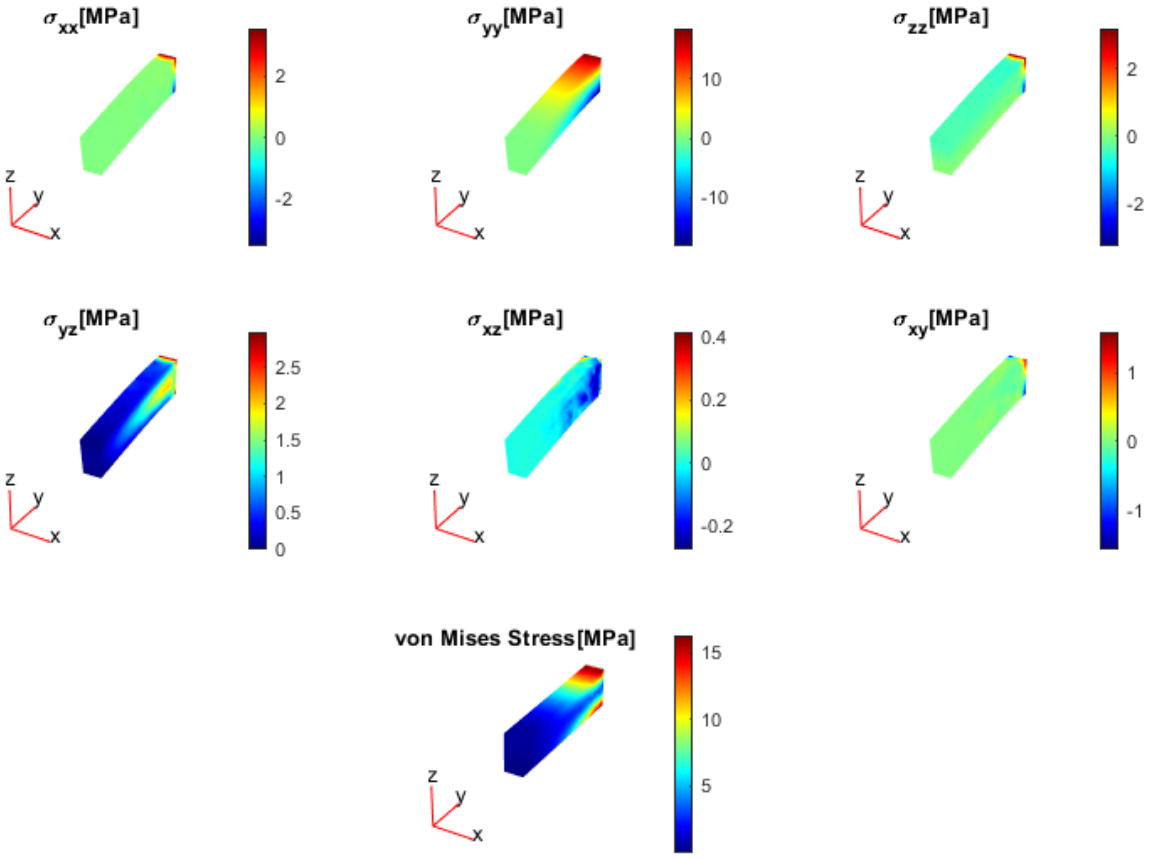

Fig. 9. Stress results of C35/45 RC cantilever beam.

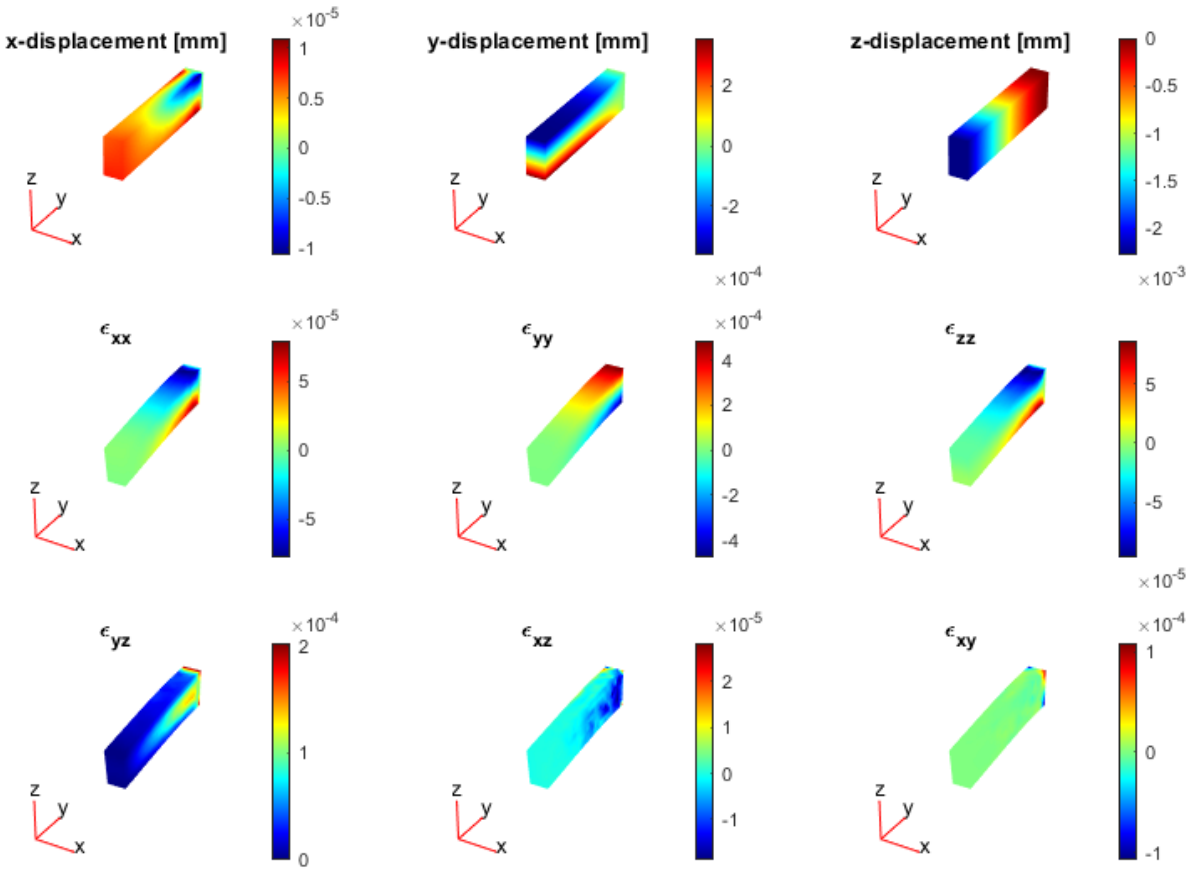

Fig. 10. Displacement and deformation results of C40/50 RC cantilever beam.

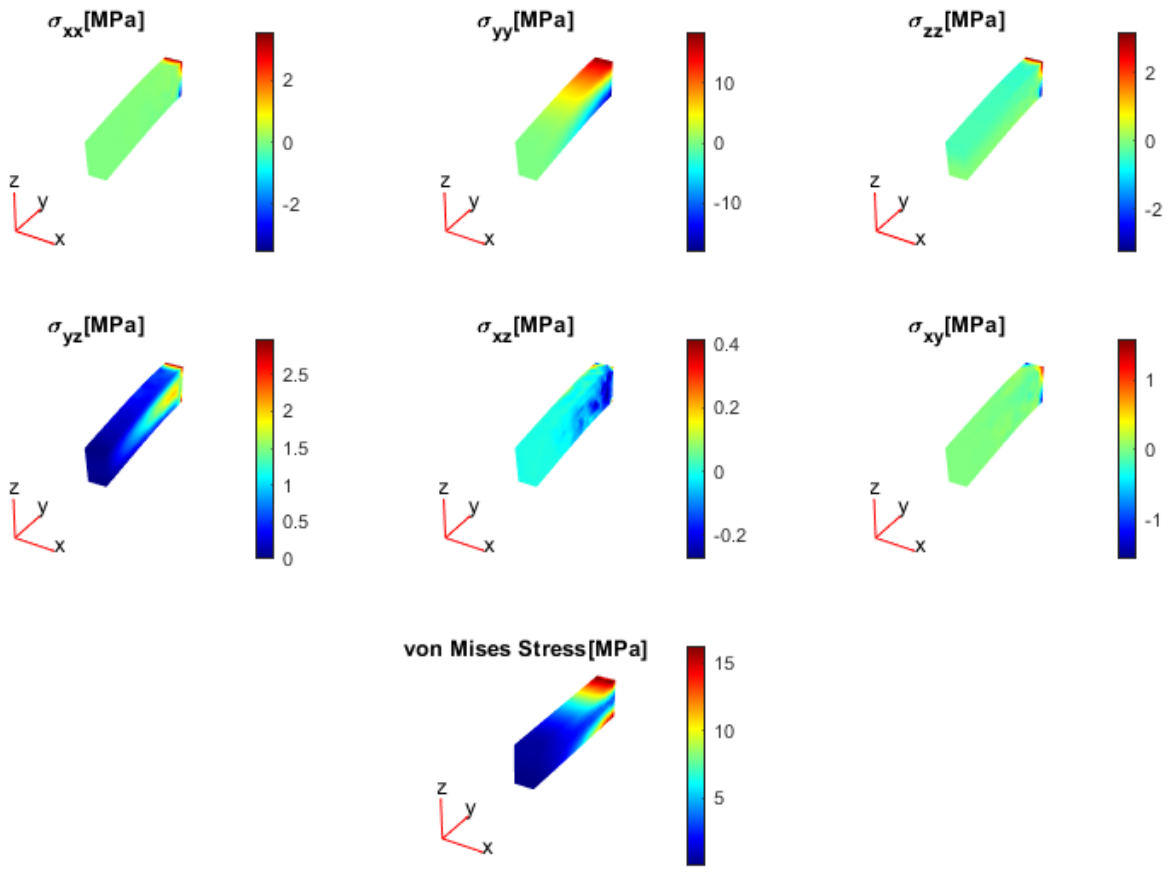

Fig. 11. Stress results of C40/50 RC cantilever beam.

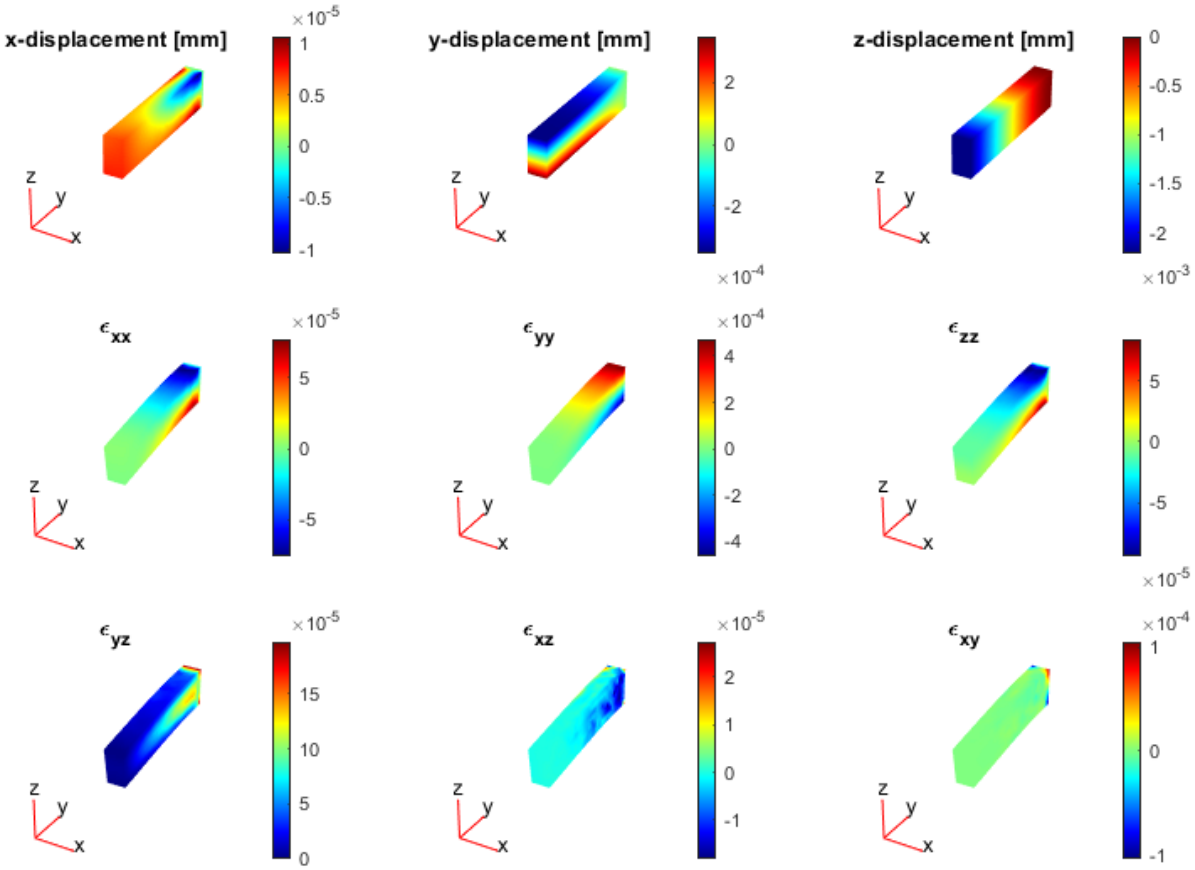

Fig. 12. Displacement and deformation results of C45/55 RC cantilever beam.

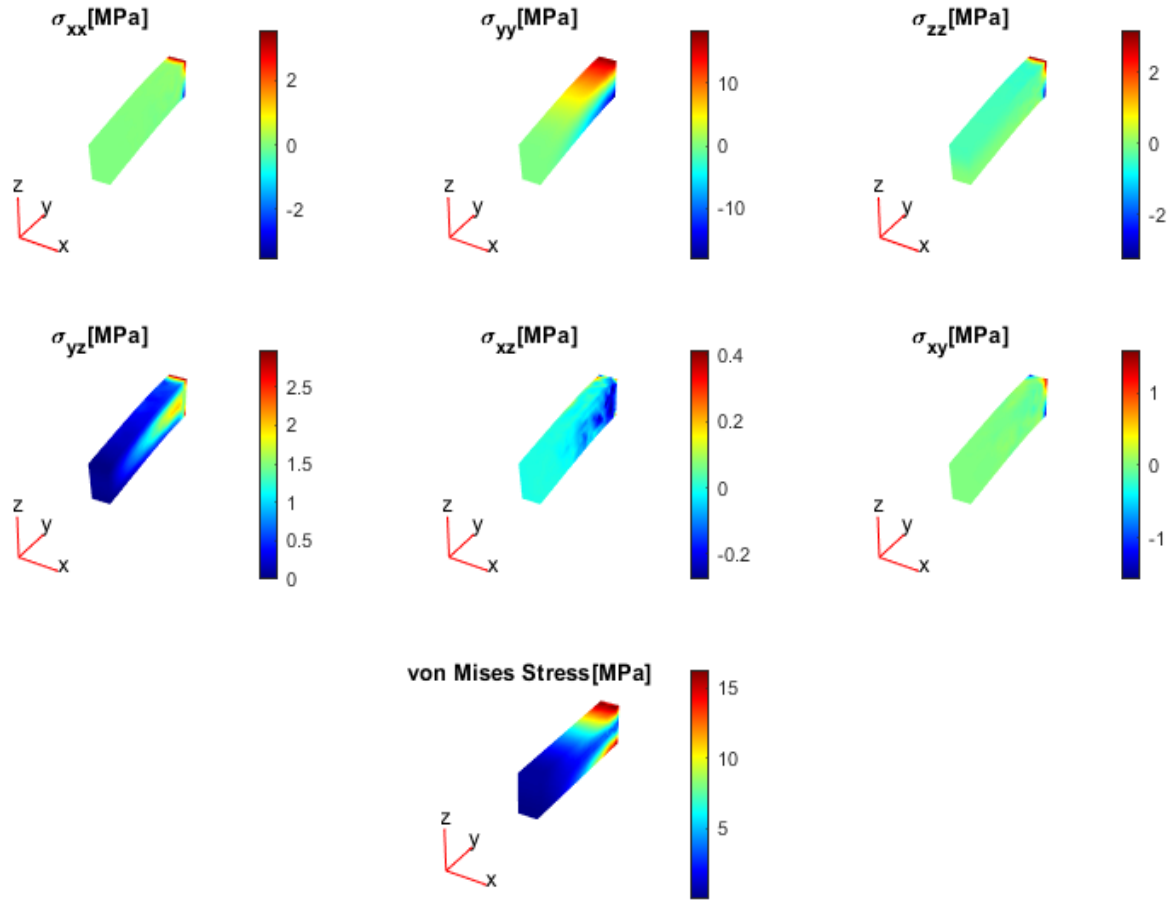

Fig. 13. Stress results of C45/55 RC cantilever beam.

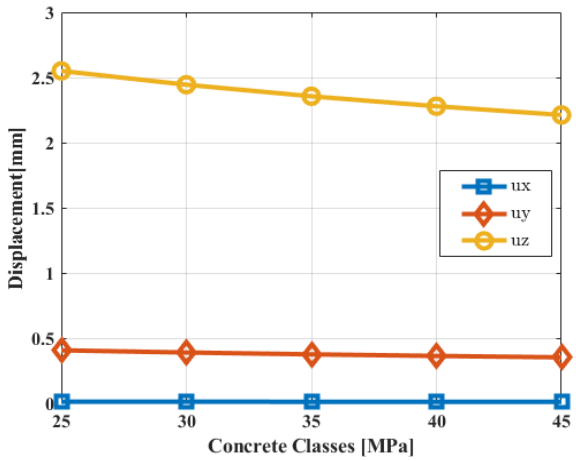

Fig. 14. The relationship of displacement (in the direction of z) with the concrete class.

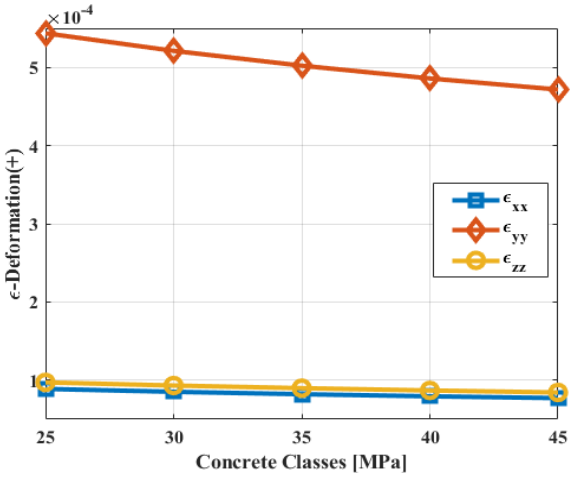

Fig. 15. The relationship of deformation (elongation in the direction of y) with the concrete class.

By examining Figs. 4, 6, 8, 10, 12 and 14 together, it can be clearly seen that the displacement in the z-axis direction (the distributed loading direction) decreases with the increase of the compressive strength of the concrete.

By examining Figs. 4, 6, 8, 10, 12 and 15 together, it can be clearly identified that the deformation (elongation) in the y-axis direction decreases with the increase in the compressive strength of the concrete.

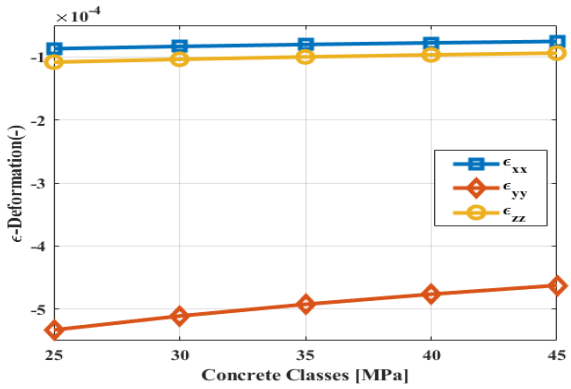

Fig. 16. The relationship of deformation (shortening in the direction of *y*) with the concrete class.

By examining Figs. 4, 6, 8, 10, 12 and 16 together, it can be deducted that the deformation (shortening) in the *y*-axis direction decreases with the increase in the compressive strength of the concrete.

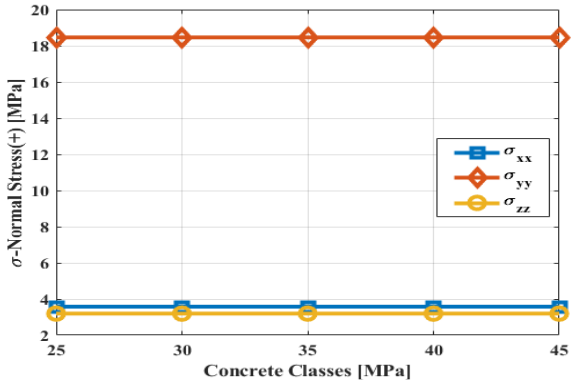

Fig. 17. Normal stress (tensile in bending) relationship with concrete classes.

Examining Figs. 5, 7, 9, 11, 13 and 17 together revealed that the normal stress (tensile in bending) in the y-axis direction remains constant with the increase in the compressive strength of the concrete.

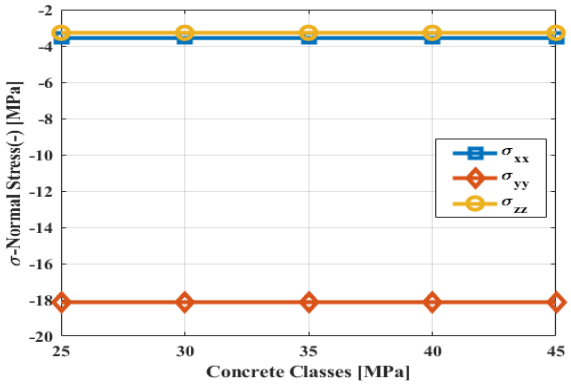

Fig. 18. Normal stress (compression in bending) relationship with concrete classes.

Examining Figs. 5, 7, 9, 11, 13 and 18 together, revealed that the normal stress (compression in bending) in the *y*-axis direction remains constant with the increase in the compressive strength of the concrete.

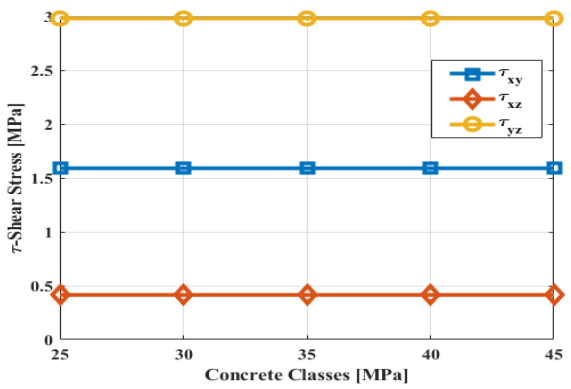

Fig. 19. Shear stress (positive) relationship with concrete classes.

By examining Fig. 5, 7, 9, 11, 13 and 19 together, revealed that the shear stress (positive) in the *xy*-axis direction remains constant with the increase in the compressive strength of the concrete.

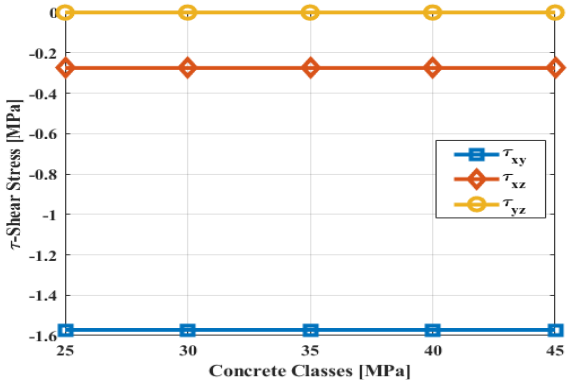

Fig. 20. Shear stress (negative) relationship with concrete classes.

By examining Fig. 5, 7, 9, 11, 13 and 20 together, it can be deducted that the shear stress (negative) in the *xy*-axis direction remains constant with the increase in the compressive strength of the concrete.

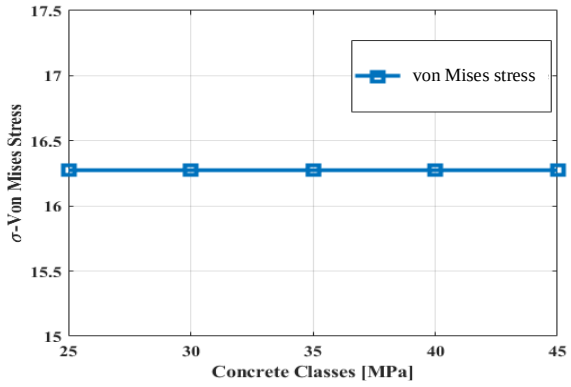

Fig. 21. von Mises stress relationship with concrete classes.

By examining Figs. 5, 7, 9, 11, 13 and 21 together, von Mises stresses seem to remain constant with the increase of the compressive strength of the concrete.

A comparison of MATLAB PDE Toolbox results and ANSYS results are provided in Tables 2-6. By examining the results for all concrete classes, it is seen that the displacement, deformation and stress values obtained from both methods are very close to each other.

Table 2. Comparison of MATLAB PDE Toolbox and ANSYS results (for C25/30 concrete class).

	MATLAB	ANSYS
Largest displacement (u_z)	2.56 mm	2.56 mm
Largest deformation (ε_{yy})	0.00054	0.00055
Largest normal stress (σ_{yy})	18.46 MPa	18.57 MPa
Largest shear stress (τ_{yz})	2.97 MPa	2.92 MPa
Largest von Mises stress	16.27 MPa	16.14 MPa
Largest von Mises strain	0.00052	0.00052

Table 3. Comparison of MATLAB PDE Toolbox and ANSYS results (for C30/37 concrete class).

	MATLAB	ANSYS
Largest displacement (u_z)	2.44 mm	2.46 mm
Largest deformation (ε_{yy})	0.000521	0.00054
Largest normal stress (σ_{yy})	18.46 MPa	18.57 MPa
Largest shear stress (τ_{yz})	2.97 MPa	2.92 MPa
Largest von Mises stress	16.27 MPa	16.15 MPa
Largest von Mises strain	0.000495	0.00049

Table 4. Comparison of MATLAB PDE Toolbox and ANSYS results (for C35/45 concrete class).

	MATLAB	ANSYS
Largest displacement (u_z)	2.35 mm	2.37 mm
Largest deformation (ε_{yy})	0.000502	0.00052
Largest normal stress (σ_{yy})	18.46 MPa	18.57 MPa
Largest shear stress (τ_{yz})	2.97 MPa	2.92 MPa
Largest von Mises stress	16.27 MPa	16.15 MPa
Largest von Mises strain	0.00047	0.00047

Table 5. Comparison of MATLAB PDE Toolbox and ANSYS results (for C40/50 concrete class).

	MATLAB	ANSYS
Largest displacement (u_z)	2.27 mm	2.29 mm
Largest deformation (ε_{yy})	0.000485	0.00050
Largest normal stress (σ_{yy})	18.46 MPa	18.57 MPa
Largest shear stress (τ_{yz})	2.97 MPa	2.92 MPa
Largest von Mises stress	16.27 MPa	16.15 MPa
Largest von Mises strain	0.00046	0.00046

Table 6. Comparison of MATLAB PDE Toolbox and ANSYS results (for C45/55 concrete class).

	MATLAB	ANSYS
Largest displacement (u_z)	2.21 mm	2.22 mm
Largest deformation (ε_{yy})	0.0004716	0.00048
Largest normal stress (σ_{yy})	18.46 MPa	18.57 MPa
Largest shear stress (τ_{yz})	2.97 MPa	2.92 MPa
Largest von Mises stress	16.27 MPa	16.15 MPa
Largest von Mises strain	0.000448	0.00045

In 15.4.9.a matter of Turkish Building Earthquake Code 2018 (Turkish Building Earthquake Code-2018 n.d.), it is specified that "Maximum compressive strain (deformation) of concrete can be taken as 0.0035 and maximum strain (deformation) of reinforcing steel can be taken as 0.01". By examining Tables 2-6, it can be seen that the deformations are below the limit values of the cited code. In addition, von Mises stresses are below the boundary stress values of the concrete (UNE EN 1992-1-2:2011/A1:2021 Eurocode 2: n.d.).

4. Conclusions

In this study, 3D static analyzes of a RC cantilever beam were carried out according to different concrete classes. Modeling and analysis of the cited beam were carried out using open source codes with the MATLAB PDE toolbox based on the FEM, and the results were compared with the ANSYS computer program. As a result of the structural analysis, displacements, deformations and stresses were obtained. It has been observed that the displacements, deformations and stresses do not exceed the standard limit values. By comparing the vertical displacement in the z-axis direction between the lowest concrete class (C25/30) and the highest concrete class (C45/50), a decrease of 18.18% has been found. Likewise, when a comparison is made for deformation (elongation) and deformation (shortening) in the y-axis direction, there is a 15.27% reduction. Moreover, when a comparison is made for normal stress (tensile and compressive in bending), shear stress and von Mises stresses, it can be identified that the values remain constant. In addition, same structural analyzes were carried out in the ANSYS program to verify the analysis results of MATLAB PDE toolbox. As a result of the validation analysis, very close values were obtained.

Acknowledgements

None declared.

Funding

The authors received no financial support for the research, authorship, and/or publication of this manuscript.

Conflict of Interest

The authors declared no potential conflicts of interest with respect to the research, authorship, and/or publication of this manuscript.

References

ANSYS (2016). ANSYS Software | ANSYS. https://www.ansys.com/products/ansys-workbench

Argyris JH, Kelsey, S (1960). A generalised discourse with applications on energy principles of structural analysis including the effects of temperature and non-linear stress-strain relations. *Energy Theorems and Structural Analysis*, 960.

Bathe KJ, Wilson EL (1976). Numerical Methods in Finite Element Analysis. Prentice Hall.

Doğangün A (2020). Betonarme Yapıların Hesap ve Tasarımı. Birsen Publishing, İstanbul.

Gallagher RH (1975). Finite Element Analysis Fundamentals. Prentice-Hall, Englewood Cliffs, New Jersey.

Jones RM (2009). Deformation Theory of Plasticity. Bull Ridge Corporation.

Kasımzade AA (2018). Finite Element Method Fundamentals and Applications in Structural Mechanics. Nobel Academic Publishing.

MATLAB R2023a (2023). https://www.mathworks.com/products/pde.html

McDowell DL, Ellis R (1993). Advances in Multiaxial Fatigue. American Society for Testing and Materials, Philadelphia.

Oden JT, Sato T (1967). Finite strains and displacements of elastic membranes by the finite element method. *International Journal of Solids and Structures*, *3*(4), 471–488.

Turkish Building Earthquake Code-2018 (n.d.). Retrieved April 17, 2023, from https://www.afad.gov.tr/

Turner MJ, Clough RW, Martin HC, & Topp LJ (2012). Stiffness and Deflection Analysis of Complex Structures. *Journal of the Aeronautical Sciences*, *23*(9), 805–823.

UNE EN 1992-1-2:2011/A1:2021 Eurocode 2: (n.d.). Retrieved April 17, 2023, from https://www.en-standard.eu

Zienkiewicz OC (1972). Finite Element Method in Engineering Science. McGraw-Hill Inc., USA.

Challenge Journal of Structural Mechanics

Research Article

Viscoelastic rod using the generalized finite difference method

Fuat Korkut [a], Turgut Tokdemir [b,*]

[a] *Department of Civil Engineering, Van Yüzüncü Yıl University, 65080 Van, Türkiye*
[b] *Department of Engineering Sciences, Middle East Technical University, 06800 Ankara, Türkiye*

ABSTRACT

The finite difference method is quite extensively used to obtain the approximate solutions of many equations of mathematical physics. In this study, the precise algorithm in the time domain is combined with the generalized finite difference method to solve dynamic viscoelasticity problems. The numerical results obtained are satisfactory, and they are presented together with finite difference and finite element solutions.

ARTICLE INFO

Article history:
Received 23 June 2023
Revised 11 August 2023
Accepted 25 August 2023

Keywords:
Finite differences
Generalized finite differences
Finite elements
Viscoelastic rod
Dynamic analysis

1. Introduction

The classical finite difference method is used to solve a large variety of engineering problems. However, when the region under consideration gets complicated, the classical method becomes difficult to apply since it involves the use of irregular grids. In many structural mechanics problems, for example large deformations, and propagation of crack, the domain's geometry changes continuously, which can make analyzing problems challenging and expensive. Meshless methods provide an alternative technique to explore these issues and eliminate mesh-related problems. The generalized finite difference method (GFDM), which is also called meshless finite difference method (Jaworska and Milewski 2016; Fu et al. 2020), on the other hand, can readily use irregular grids or clouds of points with high efficiency. This capability of the method extends its applicability to a wider range of problems. The main ideas behind this meshless method were given in the seventies. Nevertheless, fully arbitrary meshes were first used by Jensen (1972). Perrone and Kao (1975) suggested some modifications to improve the behavior of the coefficient matrix. Liszka and Orkisz (1980) introduced the use of the finite difference method at arbitrary irregular grids.

Benito et al. (2001) conducted a study to examine the impact of the primary parameters involved. In this meshless method Taylor series expansion of functions are used to compute approximations to derivatives at some specified points. These approximations are then used to solve differential equations in an approximate manner. Of course, the precision of the solution obtained can readily be improved by adding more and more terms in the Taylor series expansion and/or by adding more points into the domain.

The formulation given in the next section is for one-dimensional problems. Three terms in the Taylor series expansion are retained in the derivations. Of course, when only two terms are retained, the solution obtained would be less accurate. Generalized finite differences can easily be extended to higher dimensional problems. It is to be noted that generalized finite differences are used to integrate the governing differential equation of the problem with respect to space variables. The resulting second-order system is first converted to an equivalent system of first-order ordinary differential equations. Then the resulting system is solved using an implicit Runge-Kutta method (Radau) of order 5 with step size control (Hairer and Wanner 1991).

* *Corresponding author*. Tel.: +90-432-444-5065 ; Fax: +90-432-225-1730 ; E-mail address: author@institute.xxx (Co. Author)
ISSN: 2149-8024 / DOI: https://doi.org/10.20528/cjsmec.2023.03.004

2. Generalized Finite Difference Method

For a sufficiently differentiable function $f(x)$, defined in a region $0 \le x \le L$, the Taylor series expansion around a point $P(x_i)$ is

$$f(x) = f_i + (x-x_i)\frac{df_i}{dx} + \frac{1}{2}(x-x_i)^2\frac{d^2f_i}{dx^2} + \frac{1}{6}(x-x_i)^3\frac{d^3f_i}{dx^3} + O(x-x_i)^4 \tag{1}$$

where $f_i = f(x_i)$. One can define the error the above Taylor series expansion as $e(x) = f_i - f(x)$ and the error computed at point $Q(x_j)$ is e_j. Let $\omega(x)$ be a weighting function with compact support, then one can define norm *B*

$$B = \sum_{\substack{j=1 \\ i \ne j}}^{N} \left(e(x_j)\omega_j \right)^2 \tag{2}$$

substituting for $e(x_j)$ gives,

$$B = \sum_{\substack{j=1 \\ i \ne j}}^{N} \left[\left[f_i - f_j + (x_j - x_i)\frac{df_i}{dx} + \frac{1}{2}(x_j-x_i)^2\frac{d^2f_i}{dx^2} + \frac{1}{6}(x_j-x_i)^3\frac{d^3f_i}{dx^3} \right]\omega_j \right]^2 \tag{3}$$

where *N* is the total number of points in the region. Approximations to df_i/dx, d^2f_i/dx^2, and d^3f_i/dx^3 can be computed by minimizing norm *B*,

$$\frac{\partial B}{\partial \{Df\}} = 0 \tag{4}$$

$$\{Df\}^T = \left\{ \frac{df}{dx}, \frac{d^2f}{dx^2}, \frac{d^3f}{dx^3} \right\} \tag{5}$$

which yields a set of three equations with three unknowns for each point $P(x_i)$. These equations are

$$\begin{bmatrix} \sum \omega_j^2 h_j^2 & \sum \omega_j^2 \frac{h_j^3}{2} & \sum \omega_j^2 \frac{h_j^4}{6} \\ \sum \omega_j^2 \frac{h_j^3}{2} & \sum \omega_j^2 \frac{h_j^4}{4} & \sum \omega_j^2 \frac{h_j^5}{12} \\ \sum \omega_j^2 \frac{h_j^4}{6} & \sum \omega_j^2 \frac{h_j^5}{12} & \sum \omega_j^2 \frac{h_j^6}{36} \end{bmatrix} \begin{Bmatrix} df_i/dx \\ d^2f_i/dx^2 \\ d^3f_i/dx^3 \end{Bmatrix} = \begin{pmatrix} -f_i \sum \omega_j^2 h_j + \sum f_j \omega_j^2 h_j \\ -f_i \sum \omega_j^2 \frac{h_j^2}{2} + \sum f_j \omega_j^2 \frac{h_j^2}{2} \\ -f_i \sum \omega_j^2 \frac{h_j^3}{6} + \sum f_j \omega_j^2 \frac{h_j^3}{6} \end{pmatrix} \tag{6}$$

The above system of linear equations might be presented in matrix form:

$$A_P D_P = b_P \tag{7}$$

where A_P is a 3×3 matrix and b_P is a 3×1 vector. For computational purposes the right hand side in Eq. (6) is expressed in the form

$$b_P = B_P \tilde{f} \tag{8}$$

where *B* is a $3\times(N+1)$ matrix

$$B_P = \begin{bmatrix} -\sum \omega_j^2 h_j & \omega_1^2 h_1 & \omega_2^2 h_2 & \cdots & \omega_{N-1}^2 h_{N-1} & \omega_N^2 h_N \\ -\sum \frac{1}{2}\omega_j^2 h_j^2 & \frac{1}{2}\omega_1^2 h_1^2 & \frac{1}{2}\omega_2^2 h_2^2 & \cdots & \frac{1}{2}\omega_{N-1}^2 h_{N-1}^2 & \frac{1}{2}\omega_N^2 h_N^2 \\ -\sum \frac{1}{6}\omega_j^2 h_j^3 & \frac{1}{6}\omega_1^2 h_1^3 & \frac{1}{6}\omega_2^2 h_2^3 & \cdots & \frac{1}{6}\omega_{N-1}^2 h_{N-1}^3 & \frac{1}{6}\omega_N^2 h_N^3 \end{bmatrix} \tag{9}$$

and $\tilde{f}$ is an $(N+1)\times 1$ vector

$$\tilde{f}^T = \begin{pmatrix} f_i & f_1 & f_2 & \cdots & f_{N-1} & f_N \end{pmatrix} \tag{10}$$

Eq. (6) can be inverted to compute derivatives df_i/dx, $d^2 f_i/dx^2$, and $d^3 f_i/dx^3$ at point $P(x_i)$ in terms of nodal values of $f(x)$, that is, in terms of vector $\tilde{f}$ as follows

$$\begin{Bmatrix} df_i/dx \\ d^2 f_i/dx^2 \\ d^3 f_i/dx^3 \end{Bmatrix} = C_P \tilde{f} \tag{11}$$

where $C_P = A_P^{-1} B_P$.

3. Governing Equations

Governing equations of a dynamic viscoelastic problem are

$$\sigma_{ij,j} + F_i = \rho \frac{\partial^2 u_i}{\partial x^2} \quad x \in R \tag{12}$$

$$\varepsilon_{ij} = \frac{1}{2}\left(u_{i,j} + u_{j,i}\right) \tag{13}$$

where σ_{ij} and ε_{ij} represent stress and strain tensors, respectively, u_i is the displacement vector, ρ is the density, F_i is the body force, and R is the domain of definition of the problem. In these expressions, *i* and *j* range from one to dimension of the problem (that is to 1 for one-dimensional problems, to 2 for two-dimensional problems). The boundary conditions are specified along the boundaries of R in the form

$$u_i = \tilde{u}_i \quad x \in \Gamma_u \tag{14}$$

$$\sigma_{ij} n_j = \tilde{p}_i \quad x \in \Gamma_\sigma \tag{15}$$

where n_j is the unit outward vector, $\tilde{p}_i$ refers to the prescribed traction vector on the boundary, $\Gamma = \Gamma_u + \Gamma_\sigma$ denotes the boundary of the region R. The initial conditions are

$$u_i = \tilde{u}_i^0(x) \; at \; t = 0 \tag{16}$$

$$\frac{\partial u_i}{\partial t} = \tilde{\upsilon}_i^0(x) \; at \; t = 0 \tag{17}$$

here $\tilde{u}_i^0(x)$ and $\tilde{\upsilon}_i^0(x)$ are prescribed functions.

The stress-strain constitutive relations for isotropic viscoelastic material are given in differential form (Christensen 1982).

$$p_0 s_{ij} + p_1 \frac{ds_{ij}}{dt} + p_2 \frac{d^2 s_{ij}}{dt^2} + \cdots = q_0 e_{ij} + q_1 \frac{de_{ij}}{dt} + q_2 \frac{d^2 e_{ij}}{dt^2} + \cdots \tag{18}$$

where s_{ij} and e_{ij} are deviatoric components of stress and strain, respectively, and p_0, p_1, p_2, and q_0, q_1, q_2 are material constants.

4. Dynamic Analysis of a One-Dimensional Viscoelastic Rod

Haitan and Yan (2003) solved the one-dimensional viscoelastic rod problem using an element-free Galerkin method. Their results agree well with other solutions. For one-dimensional problems, the governing equation becomes $\sigma_{x,x} = \rho \partial^2 u/\partial t^2$. Consider a viscoelastic rod with length $L = 0.9$, density $\rho = 100$, and Kelvin model with $p_0 = 1$, $q_0 = 1$, and $q_2 = 2$ (Haitan and Yan 2003). The governing equation in terms of displacement becomes

$$q_0 \frac{\partial^2 u}{\partial x^2} + q_1 \frac{\partial}{\partial t}\left(\frac{\partial^2 u}{\partial^2 x}\right) = \rho \frac{\partial^2 u}{\partial x^2} \tag{19}$$

The boundary and initial conditions are

$$u(t,0) = 0 \tag{20}$$

$$\sigma_x = \frac{\partial u(t,L)}{\partial x} = 0 \tag{21}$$

$$u(0,x) = \tilde{u}^0(x) = 0 \tag{22}$$

$$\frac{\partial u(0,x)}{\partial t} = \tilde{\upsilon}^0(x) = 0.75\frac{x}{L} \tag{23}$$

To solve the resulting differential equation using the generalized finite differences, the finite difference mesh is to be defined first. The region from 0 to *L* is subdivided into a number of equal subregions (*Ndiv*) of length Δx defining $N = Ndiv + 2$ mesh points (nodes), *Ndiv+1* regular points, and a dummy point, point *Ndiv+2*, (which does not belong to the viscoelastic bar). The term $\partial^2 u/\partial x^2$ is to be calculated at each $P(x_i)$ for $i = 1 \cdots N$. When it is substituted in Eq. (22) gives a system of ordinary differential equations in the form

$$M\ddot{u} + C\dot{u} + Ku = F \tag{24}$$

This system needs to be modified to impose the boundary conditions given. The condition at $x = 0$ $u(t,0) = 0$ is taken into account by equating all the elements of the first column and first row of each matrix to zero and taking $M_{1,1} = 1$ and $F_1 = 0$. The other boundary condition at $x = L$ $(\sigma_x = \partial u(t,L)/\partial x = 0)$ gives an extra equation at $x = L$ which can be used to eliminate the dummy unknown $u_N = u(t, L + \Delta x)$ from the system. The resulting second order system is converted into an equivalent system of first order ordinary differential equations,

$$\dot{z} = P(t,z) \tag{25}$$

where

$$z = \begin{pmatrix} u \\ \upsilon \end{pmatrix} \tag{26}$$

$$P = \begin{bmatrix} \dot{\upsilon} \\ M^{-1}\left(F - Ku - C\upsilon\right) \end{bmatrix} \tag{27}$$

which is then solved using a Runge-Kutta type solver.

5. Numerical Results

Free vibrations of the viscoelastic rod problem is solved using GFDM. The region is divided into *Ndiv* subregions yielding *N* regular nodes. The following two weight functions are tested:

In these equations $d = \sqrt{\left(x - x_i\right)^2}$ and *dm* is the radius of the circle (radius of influence) drawn at point $P\left(x_i\right)$ which determines the points in the neighborhood of *P* affecting i^{th} equation. It observed that both weight functions yield accurate results for $dm > 4\min\left(x_{i+1} - x_i\right)$. The results obtained are given together with the finite element (FE) and finite difference (FD) solutions using similar meshes. In the finite element solutions, linear elements are used. And simplest central differences are used in the finite difference solutions. It is observed that the precision of the generalized finite differences is similar to that of finite elements and finite differences. In Fig. 1, variation of tip displacement, obtained using GFDM, with time is given for different number of mesh points. A rapid convergence is observed. Results are presented for only number of mesh points equal to 3 and 24. In Fig. 2, a GFD solution for end displacement with time is given together with a FD solution. Finally, Fig. 3 shows the tip displacement solutions for N=24 using GFD, FD, and FE methods. The figure shows that all the results obtained are in good agreement.

Polynomial weight function (quadratic)

$$\omega_i = \begin{Bmatrix} 1 - 6\left(\frac{d}{dm}\right)^2 + 8\left(\frac{d}{dm}\right)^3 - 3\left(\frac{d}{dm}\right)^4 & for\ d \le dm \\ 0 & for\ d > dm \end{Bmatrix} \tag{28}$$

Polynomial weight function (cubic)

$$\omega_i = \begin{Bmatrix} \frac{2}{3} - 4\left(\frac{d}{dm}\right)^2 - 4\left(\frac{d}{dm}\right)^3 & for \quad d \le \frac{1}{2}dm \\ \frac{4}{3} - 4\left(\frac{d}{dm}\right) + 4\left(\frac{d}{dm}\right)^2 - \frac{4}{3}\left(\frac{d}{dm}\right)^3 & for \quad \frac{1}{2}dm \le d \le dm \\ 0 & for \quad d > dm \end{Bmatrix} \tag{29}$$

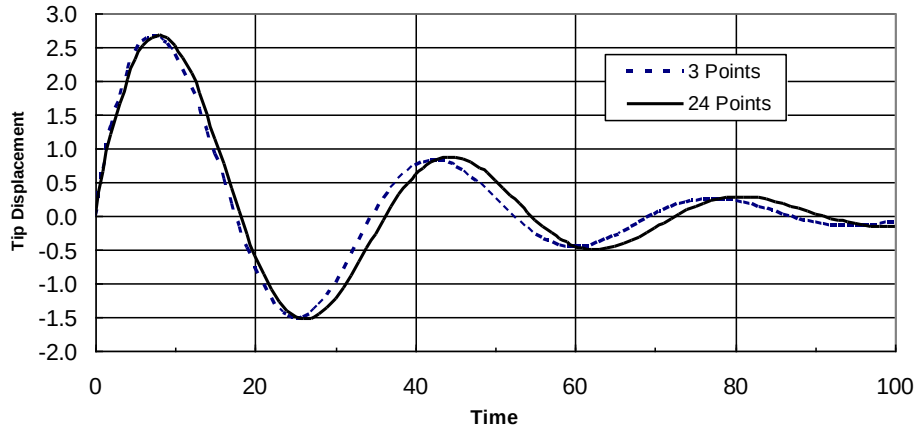

Fig. 1. The generalized finite difference (GFD) solutions for various number of nodes.

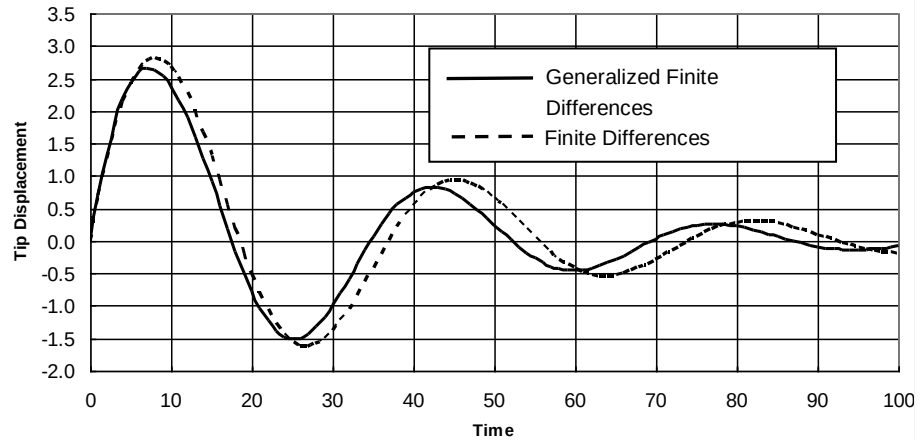

Fig. 2. The generalized finite difference (GFD) and the finite difference (FD) solutions for *N*=3.

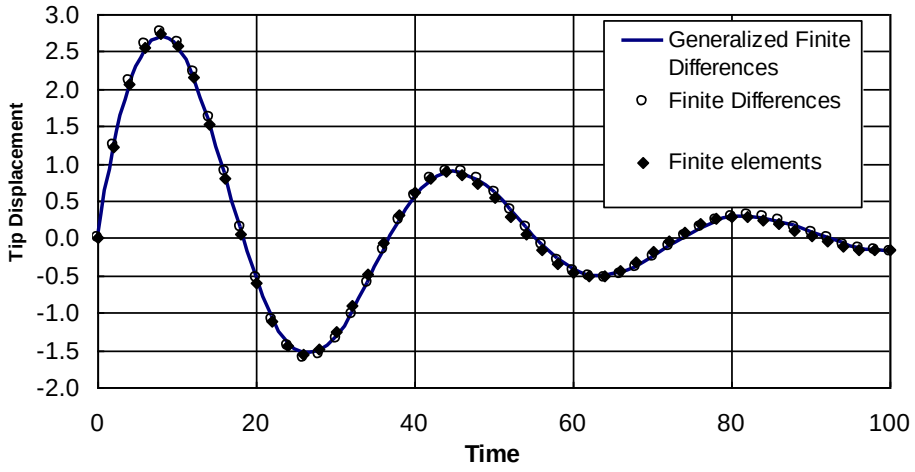

Fig. 3. Tip displacements for N=24.

6. Conclusions

GFDM has very obvious advantages over the finite element and classical finite difference methods when the domain of definition of the problem gets complicated. It is because of the fact that the GFDM does not require any element connectivity information; rather, it simply requires the coordinates of each point within the region and on its boundary together with the boundary condition information. Moreover, the type of boundary condition does not make the solution process any difficult. Both Dirichlet and Neumann-type boundary conditions can be imposed with ease. In this study, two different polynomial weight functions are tested, and it is observed that they result in solutions that are reasonably comparable. It is also observed that there is a fast improvement in the results with an increasing number of mesh points, provided that these points are evenly distributed within the region. The results obtained from GFDM, FD, and FE solutions were analyzed in this study. It is important to note that the results obtained from GFDM were observed to be strikingly similar to each other.

Acknowledgements

None declared.

Funding

The authors received no financial support for the research, authorship, and/or publication of this manuscript.

Conflict of Interest

The authors declared no potential conflicts of interest with respect to the research, authorship, and/or publication of this manuscript.

References

Benito JJ, Ureña F, Gavete L (2001). Influence of several factors in the generalized finite difference method. *Applied Mathematical Modelling*, 25 (12), 1039-1053.

Christensen RM (1982). Theory of Viscoelasticity. Academic Press, New York.

Fu ZJ, Xie ZY, Ji SY, Tsai CC, Li AL (2020). Meshless generalized finite difference method for water wave interactions with multiple-bottom-seated-cylinder-array structures. *Ocean Engineering*, 195, 1-16.

Hairer E, Wanner G (1991). Solving Ordinary Differential Equations. Stiff and Differential-Algebraic Problems. Springer Series in Computational Mathematics, Springer-Verlag.

Haitan Y, Yan L (2003). A combined approach of EFGM and precise algorithm in time domain solving viscoelasticity problems. *Journal of Solids and Structures,* 40(3), 701-714.

Jaworska I, Milewski S (2016). On two-scale analysis of heterogeneous materials by means of the meshless finite difference method. *International Journal for Multiscale Computational Engineering*, 14, 113-34.

Jensen PS (1972). Finite difference techniques for variable grids. *Computers & Structures,* 2, 17-29.

Liszka T, Orkisz J (1980). The finite difference method at arbitrary irregular grids and its application in applied mechanics, *Computers & Structures,* 11, 83-95.

Perrone N, Kao R (1975). A general finite difference method for arbitrary meshes, *Computers & Structures,* 5, 45-58.